



1 Observations of clouds, aerosols, precipitation, and surface

2 radiation over the Southern Ocean: An overview of CAPRICORN,

3 MARCUS, MICRE and SOCRATES

4 Greg M. McFarquhar^{1,2}, Chris Bretherton³, Roger Marchand³, Alain Protat^{4,5}, Paul J. DeMott⁶,
5 Simon P. Alexander^{7,5}, Greg C. Roberts^{8, 8b}, Cynthia H. Twohy^{9,8}, Darin Toohey¹⁰, Steve
6 Siems¹¹, Yi Huang¹², Robert Wood³, Robert M. Rauber¹³, Sonia Lasher-Trapp¹³, Jorgen Jensen¹⁴,
7 Jeff Stith¹⁴, Jay Mace¹⁵, Junshik Um^{1,16}, Emma Järvinen^{14,17}, Martin Schnaiter¹⁷, Andrew
8 Gettelman¹⁴, Kevin J. Sanchez⁸, Christina S. McCluskey¹⁴, Lynn M. Russell⁸, Isabel L. McCoy³,
9 Rachel Atlas³, Charles G. Bardeen¹⁴, Kathryn A. Moore⁶, Thomas C. J. Hill⁶, Ruhi S.
10 Humphries¹⁸, Melita D. Keywood¹⁸, Zoran Ristovski¹⁹, Luke Cravigan¹⁹, Robyn Schofield¹²,
11 Chris Fairall²⁰, Marc D. Mallet⁵, Sonia M. Kreidenweis⁶, Bryan Rainwater¹⁰, John
12 D'Alessandro^{1,2}, Yang Wang^{1,21}, Wei Wu¹, Georges Saliba⁸, Ezra J. T. Levin^{6,22}, Saisai Ding²³,
13 Francisco Lang¹¹, Son C.H. Truong¹¹, Cory Wolff¹⁴, Julie Haggerty¹⁴, Mike J. Harvey²⁴, Andrew
14 Klekociuk^{7,5} and Adrian McDonald^{25,26}

15
16 ¹Cooperative Institute for Mesoscale Meteorological Studies, University of Oklahoma, Norman,

17 OK

18 ²School of Meteorology, University of Oklahoma, Norman, OK

19 ³Department of Atmospheric Sciences, University of Washington, Seattle, WA

20 ⁴Australian Bureau of Meteorology, Melbourne, Australia

21 ⁵Australian Antarctic Programme Partnership, Institute for Marine and Antarctic Science,
22 University of Tasmania, Hobart, Australia

23 ⁶Department of Atmospheric Science, Colorado State University, Fort Collins, CO

24 ⁷Australian Antarctic Division, Hobart, Australia

25 ⁸Scripps Institution of Oceanography, La Jolla, CA

26 ^{8b}Centre National de Recherches Météorologiques, UMR3589, Toulouse, France

27 ⁹NorthWest Research Associates, Redmond, WA

28 ¹⁰Department of Atmospheric and Oceanic Sciences, University of Colorado, Boulder, CO

²⁹ ¹¹School of Earth, Atmosphere and Environment, Monash University, Melbourne, Australia

¹²School of Earth Sciences, University of Melbourne, Melbourne, Australia

31 ¹³Department of Atmospheric Sciences, University of Illinois, Urbana, IL

32 ¹⁴National Center for Atmospheric Research, Boulder, CO

33 ¹⁵University of Utah, Salt Lake City, UT

³⁴ ¹⁶Department of Atmospheric Sciences, Pusan National University, Busan, South Korea

35 ¹⁷Karlsruhe Institute of Technology, Karlsruhe, Germany

³⁶ ¹⁸Climate Science Centre, Oceans and Atmosphere, CSIRO, Melbourne, Australia

37 ¹⁹School of Earth and Atmospheric Sciences, Queensland University of Technology, Brisbane,
38 Australia

39 ²⁰NOAA, Boulder, Colorado

²¹Beijing Normal University, Beijing, China

41 ²²Handix Scientific, Boulder, Colorado

42 ²³Peking University, Beijing, China

43 ²⁴National Institute of Water and Atmospheric Research, Wellington, New Zealand

44 ²⁵Gateway Antarctica, University of Canterbury, Christchurch, New Zealand

²⁶School of Physical and Chemical Sciences, University of Canterbury, Christchurch, New Zealand

47 Corresponding Author

49 Greg M. McFarquhar

50 Cooperative Institute for Mesoscale Meteorological Studies

51 University of Oklahoma

52 120 David L. Boren Blvd.,

53 Norman, OK 73072
54 6 1 48

54 mcfarq@ou.edu; 405-325-3041
55

57 Submit to the *Bulletin of the American Meteorological Studies*

58 11 September 2020

59
60

ABSTRACT

61 Weather and climate models are challenged by uncertainties and biases in simulating Southern
62 Ocean (SO) radiative fluxes that trace to a poor understanding of cloud, aerosol, precipitation and
63 radiative processes, and their interactions. Projects between 2016 and 2018 used in-situ probes,
64 radar, lidar and other instruments to make comprehensive measurements of thermodynamics,
65 surface radiation, cloud, precipitation, aerosol, cloud condensation nuclei (CCN) and ice
66 nucleating particles over the SO cold waters, and in ubiquitous liquid and mixed-phase clouds
67 common to this pristine environment. Data including soundings were collected from the
68 NSF/NCAR G-V aircraft flying north-south gradients south of Tasmania, at Macquarie Island, and
69 on the RV Investigator and RSV Aurora Australis. Synergistically these data characterize
70 boundary layer and free troposphere environmental properties, and represent the most
71 comprehensive data of this type available south of the oceanic polar front, in the cold sector of SO
72 cyclones, and across seasons.

73 Results show a largely pristine environments with numerous small and few large aerosols above
74 cloud, suggesting new particle formation and limited long-range transport from continents, high
75 variability in CCN and cloud droplet concentrations, and ubiquitous supercooled water in thin,
76 multi-layered clouds, often with small-scale generating cells near cloud top. These observations
77 demonstrate how cloud properties depend on aerosols while highlighting the importance of
78 dynamics and turbulence that likely drive heterogeneity of cloud phase. Satellite retrievals
79 confirmed low clouds were responsible for radiation biases. The combination of models and
80 observations is examining how aerosols and meteorology couple to control SO water and energy
81 budgets.

82 **CAPSULE**

83 Recent air-, ground-, and ship-based observations of clouds, aerosols and precipitation over the
84 Southern Ocean are used in concert with models and satellite retrievals to provide insight into the
85 excessive absorption of solar radiation predicted by climate and numerical weather prediction
86 models.

87

88 **1. Introduction**

89 The Southern Ocean (SO) surrounding Antarctica and consisting of parts of the southern
90 Atlantic, Pacific and Indian Oceans, is one of the cloudiest places on Earth. The fractional cover
91 of low clouds (below 3 km altitude) prevalent in the warm and cold sectors of frequent extratropical
92 cyclones reaches nearly 80% year-round (Mace et al. 2009, IPCC 2013). Relative to more easily
93 sampled locations, there is a dearth of in situ observations of aerosols, clouds and precipitation
94 over the SO, especially south of 60°S. This makes it difficult to evaluate remote sensing retrieval
95 products. General circulation models (GCMs) have difficulty with simulating the present-day
96 aerosol, cloud coverage and cloud phase over the SO, with implications for anthropogenic aerosol
97 impacts and cloud feedbacks on climate (e.g., Trenberth and Fasullo 2010, Tan et al. 2016), two
98 key uncertainties in interpreting the historical climate record and projecting future climate change.

99 Numerical weather prediction (NWP) and GCMs have struggled to correctly simulate the
100 radiative budget over the SO due to low cloud biases. Most Coupled Model Intercomparison
101 Project Phase 5 (CMIP5) models predict too much shortwave (SW) radiation absorbed over the
102 SO region (Bodas-Salcedo et al. 2014, 2016; Naud et al. 2014), with impacts on ocean temperature,
103 the Southern Hemisphere (SH) jet (Ceppi et al. 2014), Antarctic sea ice trends (Flato et al. 2013)
104 and tropical rainfall (Hwang and Frierson 2013). Comparisons with satellite data indicate that
105 model radiative biases are due primarily to a lack of low and mid-level clouds in the cold sectors
106 of cyclones (e.g., Flato et al. 2013, Bodas-Salcedo et al. 2014). It was hypothesized on the basis
107 of limited observations, mainly from satellites, that GCMs might be glaciating what are in reality
108 persistent supercooled liquid clouds. Indeed, GCM simulations in which convective
109 parameterizations have been forced to produce greater amounts of supercooled liquid water (SLW)
110 have reduced SW biases (Kay et al. 2014).

111 A related motivating issue is the apparent paucity of ice nucleating particles (INPs) over the
112 SO (Bigg 1973; Burrows et al. 2013), due to it being far removed from any continental air sources;
113 INP parameterizations are based mostly on Northern Hemisphere (NH) observations. Satellite
114 retrievals of cloud-top phase indicate that SLW is more prevalent over the SO than at equivalent
115 latitudes in the NH (Choi et al. 2010; Hu et al. 2010; Morrison et al. 2011). This could be because
116 SO supercooled clouds are starved for INPs, as hypothesized by Kanitz et al. (2011) and Vergara-
117 Temprado et al. (2018).

118 A final overarching question is how droplet concentrations are regulated in SO boundary layer
119 (BL) clouds in a synoptically active environment with high winds over a biologically productive
120 ocean. The SO is a biologically unique marine aerosol environment, its pristine nature is as close
121 to pre-industrial conditions as exists on Earth, and thus represents a natural laboratory to study
122 anthropogenic aerosol indirect radiative forcing (Carslaw et al. 2013; Ghan et al. 2013). Hoose et
123 al. (2009) showed that GCMs with prognostic aerosols tended to simulate SO clouds with too few
124 droplets compared to satellite observations, making them overly susceptible to human aerosol
125 perturbations. One hypothesis is that these models underestimate marine biogenic production of
126 cloud condensation nuclei (CCN). Satellite retrievals and some previous field observations show
127 the SO has a strong summertime maximum in cloud droplet concentration N_c (Boers et al. 1996,
128 1998), CCN (Ayers and Gras 1991), and aerosol concentrations N_a (Sciare et al. 2009) correlated
129 with phytoplankton productivity. Quinn et al. (2017) found that except for the high southern
130 latitudes, sea spray contributes less than 30% to the total CCN. However, observations in the ACE-
131 1 campaign suggested that copious sulfate aerosols can be produced in the outflow of shallow
132 precipitating cumulus clouds from nucleation of marine biogenic gases (Hudson et al. 1998; Clarke
133 et al. 1998; Russell et al., 1998).

134 Thus, there is a clear need for observations to help better model the natural aerosol lifecycle
135 and mixed-phase BL cloud over the SO. Prior to the campaigns described here, cloud and aerosol
136 measurements over the SO included those listed in Table 1. But, further observations on cloud and
137 aerosol concentrations over cold waters poleward of 60°S are critical for understanding cloud
138 processes over the SO. To understand the transition of aerosols to CCN over the remote oceans, it
139 is necessary to quantify particle sources and sinks as well as processes related to their aging,
140 including the role of new particle formation in the free troposphere, generation from breaking
141 waves over the ocean, generation of biogenic particles from gas phase oceanic emissions, the role
142 of precipitation scavenging, and the effects of updrafts and dynamics on clouds.

143 Climate model evaluation, and much current knowledge of SO clouds, aerosols,
144 precipitation, and surface radiation properties is based on satellite retrievals. Satellite studies have
145 found that cloud-top SLW is more frequent over the SO (Hu et al. 2010; Choi et al. 2010; Huang
146 et al. 2012a, b; Kanitz et al. 2011; Morrison et al. 2011; Protat et al. 2014; Huang et al. 2015) and
147 Antarctic (Grosvenor et al. 2012) than over the NH, but there are significant variations between
148 satellite retrieval products in the frequency of cloud-top SLW (Delanoe and Hogan 2010; Huang
149 et al. 2015) and these retrievals tell us little about the phase of condensate below cloud top.
150 However, potential errors in cloud retrievals, particularly those related to large solar zenith angles
151 (Grosvenor and Wood 2014) and three-dimensional effects (Wolters et al. 2010; Zeng et al. 2012;
152 Cho et al. 2015) remain a concern. Additional ground-based and airborne remote sensing, and
153 airborne in-situ measurements, are therefore needed to evaluate satellite retrievals.

154 A 2014 community workshop at the University of Washington discussed these issues,
155 recognizing the need for a large international multi-agency effort to improve the understanding of
156 clouds, aerosols, precipitation and their interactions over the SO (Marchand et al. 2014). The

157 workshop served as a motivation for the proposals of separate, but integrated, projects to various
158 funding agencies in the United States and Australia. These four collaborative projects were (1) the
159 Clouds Aerosols Precipitation Radiation and atmospheric Composition over the Southern Ocean
160 (CAPRICORN) I and II research voyages of the Research Vessel (RV) Investigator, led by the
161 Australian Bureau of Meteorology (BoM), that made extensive in-situ and remote sensing
162 measurements in 2016 and 2018, respectively, (2) the 2017-2018 Measurements of Aerosols,
163 Radiation and Clouds over the Southern Ocean (MARCUS) project, during which the United
164 States Department of Energy Atmospheric Radiation Measurement Program Mobile Facility-2
165 (DOE AMF2) was deployed on the Australian icebreaker Research Supply Vessel (RSV) Aurora
166 Australis (AA) as it made resupply voyages to Australian Antarctic bases, (3) the 2016-2018
167 Macquarie Island Cloud Radiation Experiment (MICRE) acquiring surface in-situ and remote
168 sensing observations using equipment from DOE ARM, the BoM, and the Australian Antarctic
169 Division (AAD), and (4) the 2018 Southern Ocean Cloud Radiation and Aerosol Transport
170 Experimental Study (SOCRATES) using the NSF/NCAR G-V aircraft to sample clouds, aerosols
171 and precipitation from Hobart, Australia, to within approximately 650 km of the Antarctic coast.
172 Although each project was a separate effort and no formal steering committee coordinated the
173 projects, many investigators served on the advisory board of several of the projects and there was
174 much collaboration between the campaigns. There was one integrated planning workshop (2017
175 Boulder) and two integrated data workshops after the completion of the projects (2018 Boulder,
176 2019 Hobart). Data have been freely exchanged among participants, and a special collection of
177 papers in the *Journal of Geophysical Research/Geophysical Research Letters* covering all four
178 projects has been established and is expected to grow substantially over the next few years. This
179 collaboration is essential to maximize the projects' impacts. Synergistically these data provide the

180 best available measurements of the BL and free troposphere structure, together with vertical
181 distributions of liquid and mixed-phase clouds and aerosols properties, over cold SO waters where
182 SLW and mixed-phase BL clouds are frequent.

183 **2. Overview of Field Campaigns**

184 In this section, the campaigns are introduced, detailing the scientific objectives, the time
185 period of the observations, the instruments and platforms used to acquire the observations, the
186 manner in which the observations were obtained, and a broad overview of the meteorological
187 conditions sampled. The majority of the observations was obtained in a North-South curtain
188 extending from Hobart, Australia to the Antarctic coast in the Australasian sector of the SO. Figure
189 1 shows the ship tracks from CAPRICORN I, II and MARCUS, as well as the G-V flight tracks
190 during SOCRATES and the location of the ground-observing site at Macquarie Island during
191 MICRE.

192 *2.i. MICRE*

193 The DOE ARM program, the AAD and the BoM collaborated in deploying ground-
194 instrumentation to Macquarie Island between March 2016 and March 2018. Macquarie Island is
195 located at 54.5° S, 158.9° E (north of the oceanic polar front, Figure 1) and has a small research
196 station operated by the AAD that is staffed year-round, in part by BoM. The station supports a
197 variety of research activities and includes a long history of surface weather and radiosonde
198 observations (Hande et al. 2012, Wang et al. 2015).

199 The primary objective of MICRE was to collect surface-based observations of radiation,
200 precipitation, BL clouds, and aerosol properties in order to evaluate satellite datasets and to
201 improve knowledge of diurnal and seasonal variations, especially with regards to the vertical
202 structure of BL clouds. Instrumentation deployed during MICRE is listed in Table S1 (in the

203 supplement), along with time periods for which high quality observations are available for each
204 instrument in Table S2. The data include (i) passive surface radiation (solar, longwave,
205 microwave), (ii) surface precipitation rain rates, types and particle sizes, (iii) cloud radar
206 reflectivity and Doppler velocity profiles, ceilometer and lidar backscatter (including
207 depolarization) measurements (that provide information on cloud occurrence, cloud-base and top
208 height, precipitation particle size and phase, and some vertically-resolved aerosol optical
209 properties in cloud-free conditions), (iv) ground-based number concentrations of total aerosol and
210 CCN, and (v) ground-based INP number concentration and type (via filter sample analyses).

211 *2.ii. CAPRICORN*

212 CAPRICORN was a sea-based field study using the Australian Marine National Facility
213 (MNF) RV Investigator, designed to better understand interrelated aerosol-cloud-precipitation-
214 radiation processes responsible for surface SW radiation biases in global models and discrepancies
215 between satellite rainfall measurements south of 40°S (e.g., Skofronick-Jackson et al. 2017; Protat
216 et al. 2019ab). The objectives were to (i) characterize cloud, aerosol, and precipitation properties,
217 BL structure, biological production and cycling of dimethyl sulfide (DMS) in the upper ocean,
218 atmospheric composition, and surface energy budget, as well as their latitudinal variability, (ii)
219 evaluate and improve satellite products (with a focus on the NASA A-Train and NASA / JAXA
220 Global Precipitation Mission (GPM) cloud and precipitation products, and surface heat flux
221 products), and (iii) evaluate and improve the representation of these properties in the regional and
222 global versions of the Australian Community Climate and Earth-System Simulator (ACCESS)
223 model (Puri et al. 2013). A second voyage, CAPRICORN II, occurred simultaneously within the
224 same overall region (south of Australia) as SOCRATES, and included 4 flights where the NCAR
225 G-V aircraft passed over or near the RV Investigator.

226 CAPRICORN I, held 13 March 2016 to 15 April 2016 south of Tasmania, used the
227 instruments listed in Table S3. All instruments operated near 100% of the time, and characterized
228 the basic atmospheric state (~1 radiosonde per day), vertical cloud structure, including integrated
229 liquid water and water vapor contents, cloud phase, and microphysical properties (based on cloud
230 radar, lidar, and microwave radiometer measurements), and rainfall rates and drop size
231 distributions (from disdrometer and micro rain radar measurements). The aerosol size
232 distributions, morphologies and compositions, size-resolved chemical compositions and
233 hygroscopic growth factors, cloud nuclei, CCN and INP concentrations, and some gaseous
234 atmospheric compositions including DMS and VOCs, were measured. Bio-aerosol size
235 distributions, air-sea bulk and turbulent fluxes and surface energy budgets, and sub-surface oceanic
236 properties were also measured. Three CloudSat-CALIPSO overpasses were successfully
237 intersected by the ship. The on-line supplement contains more details about the CAPRICORN-1
238 voyage, including dates and locations of 5 cases when the RV Investigator was in the cold sector
239 of major cold fronts in Table S4.

240 The main limitation of CAPRICORN I was its latitude span, with no measurements
241 collected south of 55°S (Figs. 1 and 2), and the period (late austral summer – early fall, thereby
242 not providing observations in the summer season where the largest surface radiation bias is found
243 in GCMs). This motivated CAPRICORN II, where the same comprehensive set of data as
244 CAPRICORN I was collected south of 55°S during summer. CAPRICORN II was held from 11
245 January 2018 to 21 February 2018, in combination with a major oceanographic project on the RV
246 Investigator aimed at quantifying changes in water properties and circulation of the SO, and
247 measuring distributions of trace metals and isotopes in the SO and the physical, chemical, and
248 biological processes controlling their evolving distributions. The objectives were similar to

249 CAPRICORN I, with the additional aim to collect precipitation measurements within the swath of
250 the GPM dual-frequency radar. The instrumentation was similar (Table S5), with notable additions
251 of the C-band dual-polarization Doppler radar (which did not operate during CAPRICORN I) and
252 the NSF-funded contributions as part of SOCRATES that included radiosonde launches every 6 h,
253 remote sensing instruments, and INP and bio-aerosol measurements. More details about the
254 voyage and cloud types sampled are included in the on-line supplement. Seventeen cases of
255 collocated GPM observations were collected with rain, snow, and mixed-phase precipitation
256 (Table S6). The number of identified cold sectors and cold fronts traversed by the RV Investigator
257 during CAPRICORN II are listed in Table S7.

258 *2.iii. MARCUS*

259 During MARCUS the DOE AMF2 instrument package, including the Aerosol Observing
260 System (AOS) was installed on the AA as it made routine transits between Hobart, Australia and
261 the Australian Antarctic stations of Mawson, Davis and Casey, as well as Macquarie Island
262 between 21 Oct 2017 and 23 Mar 2018. MARCUS observations enhance the CAPRICORN
263 observations in that they were collected over a 5-month period centered upon the Austral summer,
264 allowing transitions from spring to fall to be observed across the 80 days of the MARCUS voyages.
265 Because the data were collected during resupply voyages, the science team had no control on the
266 timing of the voyages, nor could specific cloud types be targeted. Thus, a range of synoptic settings
267 was sampled, providing knowledge of temperature-dependent distributions of cloud properties
268 under a variety of aerosol and cloud conditions.

269 Specific objectives proposed for MARCUS were to (1) understand the synoptically-
270 varying vertical structure of SO BL clouds and aerosols, (2) quantify sources and sinks of SO CCN
271 and INPs, including the role of local biogenic sources over spring, summer and fall, (3) quantify

272 mechanisms controlling SLW and mixed-phase clouds, and (4) advance retrievals of clouds,
273 precipitation and aerosols over the SO. Parameterization development and model evaluation
274 requirements were integrated in MARCUS' design so that systematic confrontation and
275 improvement of GCMs and NWP is possible. Instrumentation deployed during MARCUS, listed
276 in Table S8, included active and passive remote sensing instrumentation, in-situ measurements of
277 aerosols, bioaerosols and INPs, trace gas measurements and meteorological measurements
278 including six-hourly radiosonde launches, rain gauges and disdrometers. The conditions sampled
279 are listed in the on-line supplement including passages through cold fronts (Table S9).

280 *2.iv. SOCRATES*

281 SOCRATES used the NCAR/NSF G-V aircraft to sample clouds, aerosols and precipitation
282 along (primarily) north-south transects south of Hobart, Australia reaching as far south as 62°S,
283 from 15 Jan to 26 Feb 2018. The G-V made in-situ measurements within the BL and free
284 troposphere, and included remotely-sensed measurements using a cloud-radar and lidar. The G-V
285 flight tracks, shown in Figure 1, were designed to target the cold sectors of cyclones where models
286 have the most trouble producing SLW, and thus were not the same for each day.

287 The overarching objectives of SOCRATES were similar to those of MARCUS, MICRE and
288 CAPRICORN. In particular, the G-V was tasked to obtain a dataset characterizing the structure of
289 the MBL and free troposphere over the SO, including observations of the vertical distribution and
290 properties of clouds and aerosols, including CCN and INPs, so that possible mechanisms to
291 explain the excessive absorbed SW radiation in models could be tested. The instruments and flight
292 paths were designed to gather statistics on aerosols and clouds as a function of latitude, and
293 included measurements over both the RV Investigator during CAPRICORN-2 and Macquarie
294 Island as explained in the on-line supplement. Table S10 lists the instrumentation installed on the

295 G-V including in-situ cloud and aerosol probes and remote sensing devices. The on-line
296 supplement also provides information about the sampling strategy that was used to execute flights
297 collecting both in-situ and remote sensing data along with a list of all the Research Flights (RFs)
298 in Table S11.

299 Figure 2 shows the normalized fraction of observations made at each latitude during the four
300 campaigns. Apart from time spent at the Australian Antarctic stations and Macquarie Island for
301 resupplying during MARCUS, there is an even sampling of latitudes during both CAPRICORN II
302 and MARCUS. Both the RV Investigator and RSV Aurora Australis spent a large time south of
303 60°S, providing a very rare and invaluable set of data over cold waters poleward of the oceanic
304 polar front. MARCUS data are unique because they provide observations over the sea ice and
305 cover more of a seasonal cycle (October-March) than CAPRICORN II, whereas CAPRICORN I
306 and II included more thorough aerosol, oceanographic, and surface energy budget measurements
307 to put cloud observations in context, and MICRE provides the longest seasonal cycle at a single
308 location. SOCRATES provides the in-situ observations that are critical for process studies and
309 evaluation of remote sensing retrievals, and they are the only direct observations of aerosols below,
310 inside and above cloud. Thus, the combination of CAPRICORN, MICRE, MARCUS, and
311 SOCRATES data are synergistic in their characterization of the latitudinal and seasonal
312 variabilities of aerosol-cloud-precipitation-radiation processes over the SO.

313 **3. Preliminary Findings**

314 Much of the initial effort since completing the projects has focused on evaluation of data
315 quality and development of higher-level data products, as well as characterizing cloud and aerosol
316 conditions over the SO. Some of the more noteworthy findings are discussed here. Integration of
317 the datasets and comparison with model simulations and satellite retrievals is starting, a necessary

318 step to evaluate mechanisms responsible for the excess absorption of solar radiation over the SO,
319 which is the overarching objective of these projects.

320 *3.i. Latitudinal Dependence/Composition of Surface Aerosols*

321 Information on the composition and latitudinal dependence of aerosols is required to
322 understand the origin of aerosols and the role of biological aerosols and sea salt on droplet
323 nucleation in different locations and seasons. Surface aerosol volatility and hygroscopicity were
324 measured during CAPRICORN I at diameters of 40, 100 and 150 nm to provide information about
325 the composition of the Aitken and accumulation modes. Figure 3 shows that the daily averaged
326 number fraction of low volatility aerosol (persisting at 250°C) in the Aitken mode was 0.22 ± 0.2
327 (mean $\pm 1\sigma$), which indicates that the Aitken mode was largely composed of secondary non-sea
328 salt sulfates. In the accumulation mode, the mean number fraction of low volatility particles was
329 0.79 ± 0.2 , indicating most particles contained a primary sea spray sourced fraction. Low volatility
330 sea spray particle number fractions, particularly the Aitken mode, increased at higher SO latitudes
331 and were associated with higher wind speeds and generally lower particle number concentrations.
332 The proportion of primary sea spray particles observed from volatility measurements during
333 CAPRICORN I was larger than that observed from BL measurements via Scanning Transmission
334 Electron Microscopy (STEM) during SOCRATES in the summer. Further information about
335 aerosol composition and hygroscopicity measurements is provided in the on-line supplement,
336 which include chemical characterization of single particle composition by scanning transmission
337 X-ray microscopy by near-edge X-ray absorption fine structure (STXM-NEXAFS). These
338 measurements show that particles in-cloud and below-cloud have very similar organic functional
339 group compositions (Fig. S6).

340 The average CN number concentrations (diameter greater than 3 nm) during CAPRICORN
341 I were $290 \pm 170 \text{ cm}^{-3}$, below typical summertime maxima (Gras and Keywood 2017, McCoy et
342 al. 2015) and hence consistent with the seasonal cycle observed at Cape Grim, with summertime
343 maxima of approximately $500 - 550 \text{ cm}^{-3}$ and wintertime minima of approximately 150 cm^{-3} . The
344 seasonal cycle in SO aerosol number is largely driven by enhanced secondary sulfate production
345 in the summer months (Gras and Keywood 2017, McCoy et al. 2015).

346 Information on surface Fluorescent Biological Aerosol Particles (FBAPs) was provided by
347 the WIBS4. It measures the fluorescence from single aerosol particles in 3 excitation/emission
348 channels for particle sizes between 0.8 and $13 \mu\text{m}$ (Toprak and Schnaiter, 2013) to deduce
349 fluorescent (i.e., biological) and total aerosol number concentrations and size distributions. During
350 MARCUS, the FBAP aerosol number concentration was rather low with a median value of 0.43
351 L^{-1} giving an average FBAP fraction of about 0.3% in the MBL at latitudes from 46°S to 68°S
352 consistent with WIBS4 measurements in other projects. The total number concentration varied
353 strongly with latitude while the FBAP concentration was rather stable with indicated minimum
354 around -56° latitude and increasing concentrations towards the north and south. Implications of
355 these results on the sources and sinks of aerosols over the SO are being examined in several
356 publications under preparation.

357 *3.ii. BL Aerosol and CCN Vary According to Origin*

358 Aerosol measurements in the BL but above the surface give more information about
359 sources and sinks of aerosols, and their role in droplet nucleation. Ambient aerosols 150 m above
360 the ocean were collected through a CVI inlet on the G-V, but without the counterflow airstream
361 that excludes small particles. Particles in two dry diameter ranges were impacted onto carbon-
362 coated nickel grids or silicon nitride windows and stored frozen for subsequent analysis by
363 analytical STEM and X-ray spectroscopy that produces elemental inorganic composition of

364 individual aerosol particles. The size ranges were about 0.1-0.5 μm and 0.5-5 μm diameter (50%
365 cut size) for particle densities of 2 g cm^{-3} at 1000 mb. Based on size distributions from the UHSAS,
366 the 0.1-0.5 μm size range comprised between 54%-93% of the aerosol accumulation-mode number
367 concentration (above the Hoppel minimum), and aerosol concentrations $>0.1 \mu\text{m}$ were similar to
368 nearby cloud droplet concentrations N_c . Thus, particles in this size range would be expected to be
369 representative of the composition of most CCN for the cases analyzed. For the data presented here,
370 heaters on the titanium inlet and stainless steel sample line were turned off to minimize losses of
371 volatile species.

372 Figure 4 shows STEM results for 6 flights after grouping particles into different types based
373 on elemental composition and morphology (Twohy and Anderson, 2008). Fig. 4a shows results
374 for each flight, while Fig. 4b shows the overall mean composition. Particles 0.1-0.5 μm in diameter
375 were dominated by sulfur-based particles (mean 69% by number). Based on the ionic composition
376 measured on the RV Investigator during CAPRICORN-II these particles were primarily acidic
377 sulfate, likely with a small contribution from methanesulfonic acid (MSA) and other organics
378 (Twohy et al., 2020). The second-most frequent particle type in this size range (mean 28% by
379 number) was salt-based sea-spray. Fig. 4b shows different types of sea-spray, which were
380 dominated by unprocessed, sodium chloride-based sea-spray particles. However, about 40% of
381 sea spray particles were enriched in sulfur and depleted in chlorine through uptake and
382 condensation of sulfur gases (McInnes et al. 1994), and a small percentage (3%) were salts
383 enriched in calcium or magnesium. Crustal and metallic particles and externally-mixed organics
384 were also detected in the $<0.5 \mu\text{m}$ population in approximately equal proportions, but were
385 together only about 3% by number. Overall these data indicate that 0.1-0.5 μm particles in the BL
386 were dominated by biogenic sulfates, with a smaller but significant contribution from sea-spray.

387 Particles $>0.5 \mu\text{m}$ (not shown) were dominated by sea-spray, with only about 2% other aerosol
388 types. Further, many sea-spray particles in the larger size fraction had detectable carbonaceous
389 coatings, which may be important in ice nucleation in the marine environment (McCluskey et al.
390 2018a). More information about the chemical composition of the organic compounds is shown in
391 the supplement.

392 Direct observations of CCN make it possible to understand how aerosols act as CCN. To
393 investigate controls of CCN, the variability in CCN spectra in the BL was characterized using a k-
394 means clustering to group into 4 clusters associated with the observed bimodality in CN and CCN
395 concentrations. Minima in the bimodal frequency distributions of number concentrations occurred
396 at approximately 750 cm^{-3} for CN and was dependent on supersaturation for CCN (Figure 5a). The
397 four clusters were characterized as follows: 1) low CN/high CCN – southerlies influenced by
398 Antarctic coastal biological productivity, 2) high CN/low CCN – westerlies over the SO
399 characteristic of recent particle formation (RPF) events with low accumulation mode
400 concentrations due to recent precipitation, 3) high CN/high CCN – similar characteristics as high
401 CN/low CCN but with condensational growth of recently formed particles to CCN sizes, 4) low
402 CN/low CCN – aerosol populations scavenged by precipitation and lack of RPF.

403 The CCN concentrations (at 0.3% supersaturation) correlated well (Fig. 5b) with the
404 overlying N_c indicating large variations in CCN over the SO exist and have an important influence
405 on cloud microphysics. The large variability in CCN led to larger than expected variability in N_c ,
406 which ranged from 10 to 449 cm^{-3} . The variation in CN concentration was also notable, ranging
407 from $115-1153 \text{ cm}^{-3}$. To understand this variability, HYSPLIT (Stein et al. 2015, Rolph et al. 2017)
408 back trajectories were performed to identify differences in source location and transport history.
409 The back trajectories for the low CN/high CCN were consistently from the south (Figure 6d) along

410 the Antarctic coast. This source location is associated with upwelling and marine biological
411 productivity that produces biogenic gases such as DMS, which can oxidize and condense to form
412 CCN-active particles (Hegg et al. 1991, Covert et al. 1992, Andreae et al. 1995, Read et al. 2008,
413 Sanchez et al. 2018). The two clusters with westerly back trajectories (Figure 6a and 6b) contained
414 the highest CN. High CN over the pristine SO are likely due to RPF aloft (Section 3.iii) and mixed
415 downward into the MBL (Sanchez et al. 2018). The high CN/low CCN cluster contained low
416 concentrations of accumulation mode particles (and consequently, small total aerosol surface area)
417 making conditions ideal for particle formation leading to high CN concentrations (Warren and
418 Seinfeld 1985, Clarke 1993, Pirjola et al 2000). While the high CN/high CCN cluster did not have
419 low accumulation mode concentrations, the spikes in CCN concentrations at the highest
420 supersaturations (Figure 5a, >0.6%) are consistent with RPF where some particles grow to CCN
421 sizes, typically through condensational growth during long residence times over the ocean (Russell
422 et al., 1998; Bates et al. 2000, Kumala et al 2004, Rinaldi et al. 2010, Zhang et al. 2014). The on-
423 line supplement offers more information on how the back trajectories were combined with
424 ECMWF reanalysis to identify relations between BL cloud fraction and particle concentration.

425 *3.iii. New Particle Formation in Free Troposphere*

426 Analysis of free-tropospheric (3-6 km) aerosol measurements from the G-V identified
427 signatures of RPF events occurring frequently across the SO, often in association with synoptic-
428 uplift. It is hypothesized that air masses rich in precursor gasses (i.e. emissions from phytoplankton
429 at the surface) undergo rapid synoptic uplift, are processed through the associated convection,
430 cleansed of coarse and accumulation mode aerosol, and released into the free-tropospheric, low-
431 aerosol surface area environment where gas-to-particle conversion is favored (McCoy et al., 2020
432 in prep). This synoptic uplift mechanism is complementary but independent from RPF occurring

433 in the outflow of SO shallow cumulus clouds documented during ACE-1 (Clarke et al., 1998). It
434 is likely both contribute to the widespread observations of high Aitken aerosol number
435 concentrations throughout the SO free troposphere.

436 A free-tropospheric sample from RF09 is used to illustrate the synoptic-uplift mechanism
437 (Figure 7). During RPF events, simultaneously low accumulation mode aerosol number
438 concentrations (from the wing-mounted UHSAS, $100 < D < 1000$ nm) and high total number
439 concentrations (from the CN counter, $D > 11$ nm) occur, indicating presence of large Aitken mode
440 concentrations. High concentrations and rapid spatial variability in CN suggests sampling of
441 particle formation bursts or air masses at different stages of nucleation (Clement et al., 2002). RPF
442 occurrences were prolific during RF09 due to a warm conveyor belt occurring west of Australia
443 and propagating south-east towards Antarctica. For statistical air-mass evolution analysis,
444 HYSPLIT (Stein et al., 2015) 72-hour back trajectories initiated at 10-minute intervals along the
445 flight path are identified by maximum CN into RPF ($CN_{Max} \geq 2500 \text{ mg}^{-1}$) and non-RPF events
446 ($CN_{Max} < 2500 \text{ mg}^{-1}$) (Figure 7b). Standard temperature and pressure corrected units (mg^{-1}) are
447 used to enable altitude invariant analysis across the campaign. The majority of these RF09 air
448 masses are RPF and have undergone recent synoptic uplift (ascent exceeds characteristic vertical
449 velocity for synoptic events, $\sim 1 \text{ cm s}^{-1}$ (Hakim, 2013)) in the previous 20-30 hours. In the 72-hours
450 before sampling, the majority of these air masses have access to the surface ($Z < 1 \text{ km}$) and the
451 precursor gases necessary for generating new particles in a low aerosol-surface area environment.
452 RF09 is characteristic of RPF events during SOCRATES and their connection to synoptic
453 uplift. The two most frequent large-scale uplift mechanisms associated with RPF events are warm

454 conveyor belts and sub-polar vortices. Volatility analysis via comparison of heated to unheated
455 CN concentrations confirms that the particles sampled during RPF events are likely composed
456 mostly of H_2SO_4 , a prominent aerosol precursor gas arising from phytoplankton emissions. It is
457 likely that the high concentrations of Aitken-mode aerosol particles produced above-cloud by these
458 RPF events are brought into the BL (Covert et al., 1996) and influence the sub-cloud CN and CCN
459 concentrations (McCoy et al., 2020 in prep; Sanchez et al., 2018) (section 3.ii). This source of
460 Aitken mode aerosol above-cloud may help to buffer SO clouds against precipitation removal,
461 sustaining higher than expected N_c (on the order of $80\text{-}100 \text{ cm}^{-3}$ between $45\text{-}62^\circ\text{S}$), and explains
462 the larger contribution of sulfur-based particles to sub-cloud CCN compared to sea-spray (section
463 3.ii, Twohy et al. 2020; McCoy et al., 2020 in prep; Sanchez et al., in prep). Evidence supporting
464 this hypothesis, the broader implications for SO cloud-aerosol interactions, and a more detailed
465 assessment of the synoptic uplift mechanism are presented in McCoy et al. (2020 in prep).

466 *3.iv. Low INP Concentrations over SO*

467 To investigate the processes giving rise to extensive SLW over the SO, not only is information
468 about CN and CCN needed, but also about INPs. INP measurements were conducted during the
469 various SO projects to define the spatial and temporal distributions of INPs over the region for the
470 first time since the comprehensive measurements of Bigg (1973). A summary of campaigns, dates
471 and INP sampling methods are given in the on-line supplement and in Table S12. Wide regions of
472 the surface marine BL were sampled south of 45°S , while INP measurements on the G-V were
473 tailored to the standard flight patterns.

474 Figure 8 gives a broad overview of the INP data sets by focusing on the IS data collected during
475 the four ship campaigns. Key findings are the large variability of, but generally very low, INP

476 concentrations at any particular latitude, a weak overall latitudinal dependence, with highest
477 concentrations near land masses (especially toward Australia), and the large discrepancy with
478 historical measurements over the region, first pointed out in the CAPRICORN I study by
479 McCluskey et al. (2018b). McCluskey et al. (2018b) demonstrated that INP concentrations were
480 up to 100 times lower during CAPRICORN I than measured by Bigg (1973) over some of the same
481 regions, that INPs were (excepting episodic events) often predominately organic in nature with
482 contributions of both heat labile and more stable organics, and that the INP content of Austral
483 summer SO seawater samples were lower than those found in Arctic seawater. These results are
484 consistent with a primary ocean sea spray source of SO BL INPs and also lower derived INP site
485 densities (INPs per aerosol surface area) for immersion freezing in SO air compared to north
486 Atlantic air masses. Using CAM-5 with constrained meteorology, McCluskey et al. (2019)
487 demonstrated that using parameterizations linking the number concentrations of mineral dust and
488 surface area of sea spray aerosols in the global aerosol model could predict the magnitude of INPs
489 observed in CAPRICORN I, and that sea spray organic INPs dominated on average, but that
490 episodic incursions of inorganic mineral dust INPs present in the middle troposphere could occur
491 and then dominate ice nucleation in the MBL. This vertical structure of compositions is
492 demonstrated in analyses of collected aerosol compositions above, below and within clouds during
493 SOCRATES (Twohy et al. 2020).

494 The INP data sets remain to be fully explored to investigate spatial, temporal and
495 compositional variabilities, through aligning with aerosol data including real-time bioaerosol and
496 Next-Generation DNA sequencing of bacteria. Those bacterial sequencing analyses have been
497 completed for aerosol samples collected on equivalent filters to the INP units during
498 CAPRICORN-2. Results reported in Uetake et al. (2020) indicate the predominance of marine

499 bacteria in the MBL during the ship campaign, confirming the pristine marine source of aerosols,
500 and thus INPs, under most circumstances in this region. Comprehensive INP data from all SO
501 studies will ultimately be normalized for use in parameterization development (see, e.g.,
502 McCluskey et al., 2018c; 2019; Vignon et al. 2020), and will serve as a basis for constraining
503 primary ice nucleation for comparison with observations of ice formation and numerical model
504 simulations of SO clouds.

505 *3.v. Clouds: In-situ observations of variability in liquid cloud droplet number concentration*

506 In-situ G-V observations allow for process studies to investigate aerosol-cloud interactions and
507 processes controlling distributions of SLW. For example, using data obtained during 4 ramped
508 ascents and descents through BL clouds, Figure 9 shows N_c measured by the CDP as a function
509 of altitude. Although all profiles were collected in a similar geographical area on 2 different days,
510 there is considerable variability in N_c , ranging from less than 50 cm^{-3} near cloud top on RF08 at
511 latitude 55.8°S to greater than 450 cm^{-3} near the top and in mid-cloud layer for the same flight
512 further south at 58.7°S . Although some lower N_c , such as concentrations of about 50 cm^{-3} seen on
513 RF04, were associated with lower wind speeds averaging 5.5 m s^{-1} , and some higher concentrations
514 of 250 cm^{-3} on RF08 at 59.9°S and up to 450 cm^{-3} on RF08 at 58.7°S were associated with larger
515 wind speeds averaging 20.5 and 22.0 m s^{-1} respectively, correlation with wind speed was not
516 always the case (e.g., low N_c of less than 50 cm^{-3} on RF08 at 55.8°S occurred when wind speeds
517 were 26.6 m s^{-1}) as updrafts, dynamics, turbulence and coupling of the cloud with the surface layer
518 can also affect N_c . Thus, while generation of sea-salt CCN caused by breaking waves associated
519 with high winds likely contribute to variations in N_c , other factors also contribute significantly,
520 such as the influence of source regions with different bioactivity on the production of CCN and
521 the degree of coupling between the surface and cloud.

522 3.vi. *Variable but prevalent supercooled water observed in-situ*

523 Although SLW dominated many BL clouds observed during SOCRATES, information about
524 ice crystals, when present, is important for understanding SLW persistence and cloud glaciation.
525 During SOCRATES ice particle number concentrations and high-resolution images were acquired
526 over a large range of temperature with optical array probes and the PHIPS probe. Using cloud
527 phase determined with a combination of in-situ cloud probes (D'Alessandro et al. 2020, In
528 preparation), Figure 10 shows the distributions of phases as a function of temperature. In some
529 instances, even the identification of phase is poorly defined (e.g., Korolev et al. 2017) as, for
530 example, there is no consensus on how many ice crystals need to be mixed within a sample volume
531 of water drops to be mixed- rather than a liquid-phase cloud. For analysis of in-situ data, the term
532 mixed-phase refers to the occurrence of a liquid mass fraction between 0.1 and 0.9 in a 1 s time
533 period as calculated using data from a combination of size-resolved and bulk mass in-situ probes.
534 In addition to the frequent presence of clouds made exclusively of SLW at very low temperatures,
535 another notable feature was the frequent observation of glaciated clouds at relatively high
536 temperature corresponding to the Hallett-Mossop (H-M) range of $-2^{\circ}\text{C} < T < -8^{\circ}\text{C}$. Figure 11
537 shows a collection of representative ice particles images captured by the PHIPS during RF02
538 between 0 and -5°C . Typical ice particle habits were needles that were frequently rimed, thus
539 acting as possible rime splintering sources in the H-M process. Smaller ($D < 100 \mu\text{m}$) pristine
540 hexagonal columns and plates were also observed that possibly grew from ice splinters (Korolev
541 et al., 2020) (Fig. 11, first row). Some of the pristine small particles were observed to have been
542 scavenged by the larger needles and needle aggregates (Fig. 11 third row, second needle from the

543 left). Occasionally, frozen drizzle droplets were detected – either as complete or sometimes as
544 fractured particles (Fig. 11, second row).

545 The presence of small horizontal scale generating cells were noted near the tops of BL
546 stratocumulus and higher cloud layers in the free troposphere. Such cells are small regions of high
547 reflectivity that frequently produce precipitation streaks below. Although such cells have been
548 observed in other environments, such as the Arctic (McFarquhar et al. 2011) and mid-latitudes
549 (Plummer et al. 2014), the cells observed over the SO had smaller horizontal scales and thus their
550 structure and properties need to be determined to understand precipitation development and cloud
551 life cycles Wang et al. (2020) provide this characterization using times when the G-V was flying
552 near cloud top. Figure 12 shows an example of their approach whereby the probability distribution
553 functions of liquid water content, total concentration, and ice water content were compared inside
554 and outside of generating cells identified by the HCR. All three parameters are higher to a
555 statistically significant degree inside the cells, but substantial liquid water and numbers of particles
556 also occur outside the cells. This shows that although the cells provide a favorable environment
557 for particle nucleation and growth, turbulent mixing at cloud top reduces the gradients inside and
558 outside of the cells. The on-line supplement gives extra information on how the combination of
559 in-situ and remote sensing measurements can be used to identify and characterize the fine-scale
560 structure of SLW, SLD, drizzle and ice crystal type.

561 The location of liquid water is of interest not only for understanding cloud microphysical
562 process and radiative properties, but also for assessing the potential hazard posed by aircraft icing
563 when the liquid is supercooled. Icing is a significant hazard for aviation, especially over the SO,
564 and is most concerning as the droplets become large enough to impact on areas not typically
565 protected by anti-icing or de-icing systems. Small cloud droplets ($D < 50 \mu\text{m}$) tend to impact on

566 forward edges of aircraft as seen in Figure 13, while larger drops tend not to freeze on impact and
567 instead flow back farther before freezing or else are heavy enough to be somewhat independent of
568 the airflow and actually impact the aircraft behind the forward edges (Figure 13b) (FAA, 2015;
569 Cober and Isaac, 2012). Known as supercooled large drops (SLD), they can accrete on the wing
570 and other important control areas of the aircraft which are outside the heated surfaces. Freezing
571 drizzle and freezing rain are examples of SLD.

572 *3.vii. Observing secondary ice production (Rime Splintering) over SO*

573 Two research flights (RF11 and RF15) during SOCRATES were dedicated to the sampling of
574 shallow cumulus clouds in the cold sector of extratropical cyclones to understand the possible
575 maintenance of SLW in those clouds. Mossop (1970) had found ample evidence of secondary ice
576 production by rime-splintering in cumuli sampled off the western and eastern coasts of Tasmania.
577 Because of the need to focus sampling at multiple levels in the same cumulus field, there was
578 insufficient time to sample the cumuli using the standard curtain flight pattern to 60°S. Thus a
579 population of cells as far south as possible, near 55° S, was identified for sampling. Thereafter the
580 G-V flew a series of constant altitude legs about 15 min long targeting the tops of actively growing
581 cells, and also sampling at and below cloud bases, and above the cloud tops, to measure aerosol,
582 CCN and INPs. These two SOCRATES flights provided clear evidence of rime-splintering, farther
583 away from land sources than documented before. Of the 34 sampled shallow cumuli occupying
584 temperatures where rime-splintering can act (-3 to -9 °C), 47% contained regions where ice crystals
585 were orders of magnitude more than the INP observed (Scott 2019). The SOCRATES airborne
586 radar data captured the cloud macrostructure needed to place the in situ microphysical data
587 collected near the cloud tops in context (Fig. 14). A complex, multi-thermal structure was common
588 in clouds exhibiting the features of rime-splintering, and lacking in clouds that only contained

589 SLW. These new data are being used to guide and constrain detailed process-level numerical
590 modeling, to understand why some SO cumuli glaciate by this mechanism, while others do not.

591 *3.viii. Himawari-8 retrievals consistent with field observations*

592 Satellite data provide both a large-scale context for interpretation of finer resolution remote
593 sensing data and in-situ measurements. The Himawari-8 satellite, developed and operated by the
594 Japan Meteorological Agency, has provided a significant advance in geostationary satellite
595 capability over the Asia-Oceania region. It provided rapid updates on meteorological conditions
596 and cloud systems throughout the SO campaigns which were especially critical for aircraft
597 operations.

598 Figure 15a shows the flight tracks of the 15 SOCRATES missions and the outermost
599 boundaries of the 15 sectors used for the Himawari-8 analysis. Figure 15b shows the frequency of
600 occurrence of Himawari-8 cloud type (Pavolonis 2010) as a function of cloud-top temperature
601 (Heidinger 2011) for the 15 SOCRATES flights. For the duration of each flight, data are taken
602 from a rectangular area that extends from 45°S to 63°S and covers the entire width of the flight
603 track. The statistics represent the overall atmospheric and cloud conditions sampled during both
604 the in-situ and remote-sensing sampling legs. Figure 15 highlights the prevalence of SLW cloud
605 tops for $0^{\circ}\text{C} > T > -25^{\circ}\text{C}$. More details of this Himawari-8 cloud classification can be found in
606 Huang et al. (2019), and information about how the in-situ cloud properties are being used to
607 evaluate cloud microphysical properties is included in the on-line supplement.

608 *3.ix. Radiative Fluxes Confirm Bias in Climate Models*

609 Many studies involving surface radiative fluxes rely on fluxes retrieved from satellites,
610 primarily from the Clouds and the Earth's Radiant Energy System (CERES) instruments or derived
611 from spaceborne cloud radar and lidar observations (CloudSat-CALIPSO). Based on CERES data,

612 most climate models participating in CMIP5 had excessive SW radiation reaching the surface over
613 the SO (Zhang et al. 2016). An evaluation of CERES Synoptic (SYN) and Energy-Balanced and
614 Filled (EBAF) Edition 4 and CloudSat retrieved surface SW and longwave (LW) downwelling
615 fluxes against surface observations collected during MICRE (Hinkelmann and Marchand 2020)
616 finds that the overall biases in the CERES-surface fluxes are modest, but slightly larger at
617 Macquarie Island than at most other locations, approximately $+10 \text{ Wm}^{-2}$ for the SW and -10 Wm^{-2}
618 for the LW in the annual mean. The SW bias is positive meaning that climate model biases in
619 downwelling SW fluxes are, if anything, slightly larger than previous studies suggest because
620 CERES downwelling fluxes may be a bit too large and models fluxes are larger yet. However,
621 both the SW and LW bias have significant seasonal and diurnal variations, with SW biases being
622 near $+20 \text{ Wm}^{-2}$ during the SH summer. Biases in LW fluxes are much larger at night (-16 Wm^{-2})
623 than during the day ($< 2 \text{ Wm}^{-2}$) with significant seasonal variations controlled by the relative ratio
624 of daytime vs. nighttime, and consequently are largest during the SH winter. This thus confirms
625 that the climate model biases that motivated the projects are indeed real.

626 *3.x. Low Clouds Responsible for Much of Climate Model Bias*

627 Understanding the contributions of different cloud types to the surface SW radiation bias
628 in models is a major objective of these field campaigns, which complements the analysis of large-
629 scale environments most conducive to such biases. Figure 16 shows the observed and modelled
630 surface cloud radiative effect (CRE) during CAPRICORN I for different cloud cover types using
631 the BoM ACCESS-C3 numerical weather prediction system (4 km horizontal resolution, no data
632 assimilation, downscaled from the regional 12-km resolution model), which was run for the
633 campaign period. The observed CRE is the difference between the measured downwelling
634 radiative flux at the surface and the simulated clear-sky downwelling radiative flux, accounting

635 for ocean albedo and the broadband infrared emissivity of seawater (e.g., Protat et al. 2017). Over
636 the CAPRICORN I period, the mean SW CRE was -66.7 Wm^{-2} , partially offset by a mean LW
637 CRE of 44.4 Wm^{-2} , resulting in a mean net CRE of -22.3 Wm^{-2} (Figure 16d). A 1-minute merged
638 cloud radar - lidar product from ship-based measurements was used to classify the observed cloud
639 profiles into different cloud cover types (Noh et al., 2019) at 1 h resolution to compare with model
640 outputs. Hours that contained only clear skies were classified as clear. Hours that contained more
641 than 30 minutes of clear skies were classified as “mostly clear”. Because the cloud cover types
642 containing clouds overlapping low, mid and high-altitude slabs made up only 5% of all the
643 observations, they were grouped into a “thick” cloud type classification. Hours that contained at
644 least 15 minutes of precipitating clouds were classified as precipitating, even if one of the other
645 conditions was met. Lastly, hours that did not meet any of these conditions were classified as
646 “mixed”.

647 During CAPRICORN I, 51% of the 697 observation hours were characterized by low
648 clouds, followed by multilayer (14%), precipitating (10%), mostly clear (10%), mixed (8%), thick
649 (5%), and clear conditions (2%). Large negative SW CREs are observed for precipitating,
650 multilayer and low cloud categories and these correspond to a mean positive SW CRE bias for all
651 three clouds types, meaning too much SW flux is reaching the surface in the model under these
652 conditions (Figure 16a). The negative SW CRE and positive SW CRE bias was partially offset by
653 positive LW CREs and a negative LW CRE bias for these cloud types (Figure 16b). This resulted
654 in a net negative CRE and a positive net CRE bias for precipitating, multilayer and low clouds
655 (Figure 16c). While smaller negative (positive) SW (LW) CREs were observed for the other cloud
656 types, the CRE biases for these had little impact on the overall CRE and CRE bias once weighted
657 by their respective frequency of occurrence (Figure 16d). For the measured SW, LW and net CRE,

658 low clouds were responsible for just over half of the total contribution during CAPRICORN I,
659 with most of the remaining contributions from multilayer and precipitating clouds. Interestingly,
660 however, low clouds were responsible for nearly all of SW, LW and Net CRE biases in ACCESS,
661 highlighting again the need to focus our attention on better understanding these low clouds. This
662 work is being extended to include the MARCUS, MICRE and SOCRATES observations.

663 *3.xi. Remote Sensing Data also shows prevalence of supercooled water*

664 The on-line supplement summarizes previous studies that have used the CAPRICORN and
665 MARCUS data to determine the frequency of and sources of SLW over the SO. To further
666 understand processes responsible for the production and maintenance of SLW over the SO, and to
667 understand the seasonal and latitudinal dependence of cloud properties, the MARCUS cloud
668 retrievals were combined with a value added product developed to describe the environmental
669 quantities at the position of the AA at 10-min resolution. Parameters examined include ship
670 navigation parameters, local meteorological conditions, SST, location of the AA relative to the
671 oceanic polar front, lower tropospheric stability, marine cold air outbreak index, inversion height,
672 lifting condensation level, location relative to the center of the nearest cyclone, warm front and
673 cold front and location of air parcels 72 hours prior to their arrival at the ship computed from
674 HYSPLIT. Consistent with prior satellite retrievals, the MARCUS data show that low-level liquid
675 water clouds are ubiquitous over the SO and that much of the water is supercooled. For instance,
676 south of 60°S over 49% of non-precipitating clouds had cloud base $T < 0^{\circ}\text{C}$ and mean liquid water
677 paths greater than 50 g m^{-2} as measured by the microwave radiometer. Figure 17 shows an example
678 of the analysis illustrating how the properties of single-layer, non-precipitating clouds with bases
679 less than 3 km and greater than 500 km away from the nearest cyclone center varied depending on
680 whether the measurements were made north or south of 60°S. The retrievals show that with average

681 cloud base T of about -10°C south of 60°S and hence the location of the oceanic polar front, SLW
682 must extensively exist even though there is less precipitable water than north of 60°S . Further,
683 CCN concentrations and retrieved N_c peaked in December, but there were large variations over all
684 seasons. Similar ongoing analysis is quantifying the dependence of cloud properties on
685 environmental and aerosol conditions, from which processes responsible for SLW can be better
686 elucidated.

687 *3.xii. Precipitation observations*

688 Recent evaluation studies of satellite rainfall products have highlighted large statistical
689 discrepancies (up to a factor 2) in zonal precipitation averages derived from GPM, CloudSat, and
690 the Global Precipitation Climatology Project (GPCP) south of 40°S and north of 40°N (Grecu et
691 al. 2016; Skofronick-Jackson et al. 2017). Shipborne disdrometer and active remote sensing
692 observations collected during CAPRICORN have been used along with others from several
693 research vessels as part of the OceanRAIN project (Klepp et al. 2018) to establish whether these
694 differences between satellite rainfall products are driven by latitudinal differences in statistical
695 properties of the drop size distribution (DSD) and associated assumptions in GPM radar rainfall
696 retrievals. Results from these investigations are summarized in Protat et al. (2019ab). A large
697 natural, latitudinal, and convective-stratiform variability of the DSD was clearly found, with a
698 much lower drop concentration for diameters smaller than 3 mm and a very different modal value
699 of the DSD shape parameter distribution (μ) to that assumed in the GPM algorithms in the SH
700 high latitude (south of 45°S) and NH polar latitude (north of 67.5°S) bands (Protat et al. 2019a).
701 From a radar rainfall retrieval perspective, the attenuation – reflectivity, drop diameter –
702 reflectivity, and rainfall rate – reflectivity relationships in the SH high latitude and NH polar
703 latitude bands are found to be fundamentally different from those at other latitude bands, producing

704 smaller attenuation, much larger drop diameters, and lower rainfall rates for a given reflectivity,
705 which potentially explains the observed discrepancies between satellite rainfall products (Protat et
706 al. 2019b). Evaluations of CloudSat and other satellite precipitation datasets using MICRE and
707 SOCRATES datasets are underway, and will be reported in future publications.

708 *3.xiii. Unique view of BL Structure from Soundings*

709 Across the four field campaigns, a total of 2,186 soundings were obtained. While a variety
710 of spatial and temporal biases exist in the sampling, the collection provides an unprecedented view
711 of the thermodynamic structure of the lower troposphere across the SO. A simple k -means cluster
712 analysis on the lower thermodynamic variables (T, relative humidity, winds (u and v) at 700, 850
713 and 925 hPa levels and surface pressure, T, and relative humidity) (Lang et al. 2018) produces a
714 cluster along the Antarctic coast (C2), another at high latitudes (C1, 55-65°S), where polar meso-
715 vortices are commonly present, and multiple clusters at lower latitudes across the SO storm track
716 (40-60°S). Increasing the numbers of clusters effectively isolates different sectors of the mid-
717 latitude storm track. For brevity the storm track clusters are merged into a single cluster (M).

718 The composite soundings for M, C1 and C2 (Figure 18a-c) illustrate differences in the
719 thermodynamic structure of the atmosphere across the SO. The M composite features strong
720 westerly winds and a low-level inversion near 900 hPa. BL clouds are commonly observed across
721 this region. C1 covers the region where the greatest bias exists in the regional energy budget
722 (Trenberth and Fasullo 2010) and it is also the region where multi-layer clouds are commonly
723 detected by A-train satellites (Mace et al. 2009). For the C1 composite (Figure 18b), the low-level
724 winds are very weak and the atmosphere is near saturation at all altitudes. A more complete
725 analysis of individual soundings (not shown) confirms that multi-layer clouds are frequent, but
726 relatively few inversions are present, which suggests that the polar meso-vortices mix the lower

727 free troposphere and that the weak winds may allow for a radiative equilibrium to weaken
728 inversions. Finally, along the Antarctic coast (C2), the composite reveals a very dry, cold
729 atmosphere, commonly cloud free. An illustrative back trajectory (Figure 18d) illustrates that the
730 low-altitude dynamics may be dominated by strong Antarctic outflows such as katabatic winds
731 draining cold, dry air off the Antarctic plateau onto the SO. Using a cyclone tracking algorithm
732 (Lim and Simmonds 2007) on the ERA5 reanalysis, we plot the location of the soundings, by
733 cluster, to the nearest cyclonic core (Figure 18e). The M soundings typically reside to the north of
734 core, the C1 soundings commonly reside just poleward of the core, while the C2 soundings reside,
735 on average, about 5° south of polar meso-vortices (Truong et al. 2020).

736 *3.xiv. Impact of Biological Particles on CCN/Droplet Concentrations near Antarctica*

737 The on-line supplement summarizes the use of remote sensing data to derive cloud
738 microphysical properties (Mace and Protat 2018; Mace et al. 2020). In Figure 19, a time series of
739 daily mean N_c retrieved from non-precipitating liquid MBL clouds during CAPRICORN II is
740 shown. The N_c represents the mean value from an entire 24 hour period with the error bars showing
741 the standard deviation of the total number of successful retrievals for that day where each retrieval
742 is valid for a 30-second interval (Figure 19e). The latitude of the ship during the 24 hour period
743 is shown in Figure 19d. N_c decreases steadily from $> 100 \text{ cm}^{-3}$ as the RV Investigator travelled
744 south through the Tasman Sea to about 50 cm^{-3} as the ship passed into the latitudes of the Antarctic
745 Circumpolar current. N_c increased by about a factor of 2 occurs on 29 January as the ship passed
746 poleward of 64°S . N_c remained elevated while the RV Investigator worked along the Antarctic
747 shelf south of 60°S . Poor weather precluded retrievals until 13 February when N_c was again found
748 to be in the 50 cm^{-3} range with the ship working back north of 60°S . N_c did not climb as rapidly
749 with latitude moving northward towards Tasmania.

750 The daily mean N_c is correlated ($r=0.48$) with daily averages of sulfate and particulate
751 methanesulfonic acid (MSA) concentrations, but N_c is less well correlated with CCN at 0.65%
752 super saturation measured at the surface ($r=0.38$). It was also found (not shown) that N_c is
753 negatively correlated ($r=-0.51$) with chloride concentrations. What is reasonably striking in Figure
754 19 is that N_c , MSA and CCN all increase substantially poleward of 60 S. Because MSA is a marker
755 of DMS oxidation, it is concluded that the higher CCN concentrations in this region are likely
756 driven by the biologically productive latitudes along the Antarctic shelf. It is plausible that this
757 effect is in line with previous observations by Humphries et al. (2016) where increased secondary
758 aerosol formation was observed south of these latitudes.

759 *3.xv. Models Test Ubiquitous Supercooled Water and Role of Biological Particles over SO*

760 Global-scale, regional-scale, and process-scale modelers were entrained into the SO
761 projects as they were designed. Scientists using the atmospheric component of NCAR's
762 Community Earth System Model version 2 (CESM2) (Danabasoglu et al., 2020) and GFDL's AM4
763 (Zhao et al. 2018) global models participated. The Australian ACCESS model (Puri et al. 2013)
764 was used for operational forecasting during SOCRATES, and its icing products were evaluated.
765 Australian and U. S. groups ran the Weather Research and Forecast (WRF; Skamarock et al. 2005)
766 regional model. A large-eddy simulation (LES) model (Atlas et al. 2020) was run with a very fine
767 grid over small domains for selected cases, as was an idealized cloud-resolving model (CM1;
768 Bryan and Fritsch 2002) for process-level studies. Table S13 lists some modeling groups that
769 participated in the projects, as well as the approximate grid resolution; additional details about the
770 LES simulations are also included in the on-line supplement. Two particular foci of the modeling
771 studies were to test hypotheses that (a) the GCMs/NWP models were too quickly glaciating clouds

772 that are in reality persistent SLW clouds, and (b) marine biogenic processes help sustain the natural
773 aerosol population over the SO.

774 From the start, the modeling team proposed a nudged-meteorology strategy (e. g. Wu et al.
775 2017) to effectively compare the global model with aircraft or ship data in the synoptically active
776 SO. As implemented, three-dimensional model fields of horizontal wind, temperature and surface
777 pressure were nudged toward a global reanalysis with a 24 hour relaxation timescale. The
778 simulated humidity, cloud and aerosol fields freely evolve and can be usefully compared with in-
779 situ observations. Ideally, the temperature and wind fields from the nudged simulations and from
780 the reanalysis to which they are being nudged should closely match corresponding observations.
781 This was found to hold remarkably well. For instance, aircraft-measured temperatures were
782 typically within 1 K of the reanalysis and within 2 K of the nudged GCMs. Fig. 5 of Gettelman et
783 al. (2020) shows the example of RF07, in which CAM6 is nudged to the MERRA2 reanalysis.
784 Both MERRA2 and the ERA5 reanalysis used by the nudged AM4 are fine choices for the nudged-
785 meteorology approach. ERA5, which input the G-V dropsonde data, was on average about 20%
786 closer to SOCRATES-observed temperature and winds than MERRA2. In addition, the regular
787 radiosonde observations made during MARCUS have been found to improve the forecast track of
788 a mid-latitude low pressure system (Sato et al., 2018).

789 Figs. 10 and 14 of Gettelman et al. (2020) show examples of comparisons of nudged
790 versions of CAM6 and its predecessor version CAM5 with aircraft cloud microphysical
791 observations from SOCRATES RF07. These show that CAM6 correctly simulates a BL
792 stratocumulus layer that is observed to be primarily supercooled liquid, while CAM5 incorrectly
793 simulates the same cloud layer to mainly be ice. CAM6 is also able to represent the structure of
794 the hydrometeor size distributions (Figure 20, adapted from Figure 9 of Gettelman et al 2020) ,

795 but with biases remaining in the representation of the peak liquid size distribution, and in excessive
796 warm rain. These detailed comparisons allow a new process understanding of weather and climate
797 models from the in-situ microphysical to the climate scale (Gettelman et al 2020).

798 Both the NSF G-V used in SOCRATES and the RV Investigator in CAPRICORN II
799 gathered extensive vertically-pointing lidar and 94 GHz cloud radar datasets that sampled entire
800 atmospheric columns. Both the CAM6 and AM4 models include implementations of the COSP
801 simulator (Bodas-Salcedo et al. 2011), which includes a 94 GHz radar simulator. This enables a
802 comparison between these powerful remote sensing datasets and the nudged-meteorology GCMs,
803 discussed at length by Zhou et al. (2020). Their Fig. 12 shows such a comparison with the RV
804 Investigator radar data for 1-15 Feb. 2018. This is a sensitivity test of the model cloud
805 microphysics and representation of precipitation. It shows CAM6 has good skill, while AM4
806 greatly underestimates snow reflectivity because its assumed snow particle size is too small. The
807 ship radar often sampled precipitating clouds which the aircraft did not target (and which were
808 often precluded by icing hazard), so it provides complementary information to the in-situ data.

809 **4. Summary and Future Work**

810 Motivated by a pressing issue on the absorption of too much solar radiation over the
811 Southern Ocean (SO) (due to problems simulating low-altitude supercooled liquid clouds) by
812 leading climate and numerical weather prediction models, a coordinated multi-agency effort
813 consisting of four field campaigns was held in the time period of 2016 to 2018. The experimental
814 design, platforms, and instruments from four experiments have been summarized here: the ground-
815 based Macquarie Island Cloud Radiation Experiment (MICRE) collecting information on surface
816 aerosol properties in-situ, and clouds, precipitation and radiation using remote sensors; the Clouds

817 Aerosols Precipitation Radiation and Atmospheric Composition over the SO (CAPRICORN) I and
818 II cruises of the RV Investigator that collected aerosol, in-situ and oceanographic measurements
819 in-situ and remotely; the Measurements of Aerosols, Radiation and Clouds over the Southern
820 Ocean (MARCUS) campaign that collected in-situ aerosol and remote sensing observations using
821 instruments installed on the icebreaker RSV Aurora Australis as it made resupply voyages from
822 Hobart to the Australian Antarctic stations and Macquarie Island; and the Southern Ocean Cloud
823 Radiation Transport Experimental Study (SOCRATES) that collected data with the NCAR/NSF
824 G-V aircraft in a north-south direction south of Hobart, Tasmania to approximately 62 S. These
825 data characterize the synoptically and seasonally-varying vertical structure of the SO BLand free
826 troposphere, including the properties of clouds and the variability and sources and sinks of
827 aerosols, cloud condensation nuclei and ice nucleating particles, to a much greater extent than was
828 previously available.

829 The experiments were designed to be complementary in how they contribute to studies of
830 processes, latitudinal variability, seasonal variability, validation of remote sensing retrievals and
831 model evaluation and improvement. MICRE gives a long seasonal record in a single location,
832 CAPRICORN I and II give the most complete ship-borne oceanographic, aerosol and surface
833 energy budget observations, MARCUS covers a longer seasonal cycle than CAPRICORN, and
834 SOCRATES provides the detailed in-situ observations that are required for process-oriented
835 understanding. Combined these data represent the most comprehensive set of data collected on
836 aerosols, clouds and precipitation over the SO over seasonal cycles, especially over cold sectors
837 of extratropical cyclones and at latitudes below 60°S where climate model biases are largest. The
838 related modeling studies tested hypotheses on the cloud processes that lead to the ubiquity of

839 supercooled clouds and the marine biogenic processes that sustain the natural aerosol population
840 over the SO.

841 Some first findings from the field campaigns addressing their overarching objectives have
842 been presented here, and are being elaborated upon in several more focused scientific articles.
843 Initial findings included that low clouds were responsible for nearly all the radiative biases in the
844 Australian forecast model ACCESS and the presence of a pristine environment with numerous
845 small and few large aerosols above cloud, highlighting the role of new particle formation in the
846 troposphere and the long-range transport from continents. There is a dearth of INPs (much lower
847 than suggested by much earlier measurements by Biggs 1973) which is a significant factor leading
848 to the ubiquitous presence of supercooled liquid water over the SO. Most INPs appear to have a
849 biological source and better understanding of secondary ice nucleating processes related to these
850 particles is needed. Further, there was a suggestion that the higher CCN concentrations south 60°
851 S were likely driven by biologically productive latitudes along the Antarctic shelf, but that sea
852 spray may have more important roles in other latitudinal bands. In the cold dry sectors of cyclones,
853 supercooled liquid water with contents as high as about 0.8 g m^{-3} were observed in very thin layers
854 at temperatures as low as -30°C and was frequently associated with the presence of narrow cloud-
855 top generating cells. Evaluation of satellite datasets is ongoing, but early results suggest the
856 CERES shortwave fluxes and imager-based (Himawari and MODIS) retrievals for low cloud
857 microphysical properties for stratocumulus are reasonably good, and pointing towards ways in
858 which retrievals of precipitation and cloud-phase among other may quantities might be refined or
859 improved. Finally, ongoing modeling and observations studies are examining how CCN properties
860 are coupled with aerosol properties and meteorological conditions, in order to provide a process-

861 oriented understanding that can be used to improve the performance of models at a variety of
862 spatial and temporal scales.

863 In terms of the motivating goal, namely the overprediction of solar radiation over the SO,
864 the hypothesis that SLW is ubiquitous is confirmed. Although measurements verified that there
865 was a dearth of INPs over the SO, the exact mechanisms by which SLW persists over the SO, and
866 the interplay of aerosols, dynamics and meteorology in this persistence are still somewhat
867 uncertain. Now that all data have been processed and conditions over the SO have been
868 characterized, integration of different data sets and comparison against models and satellite
869 retrievals is proceeding rapidly which should lead to a more integrated view of the abundance of
870 supercooled water and its role in reflecting solar radiation to reduce the observed radiative bias.

871 Inevitably, the collected data sets have limitations with their temporal and spatial coverage.
872 Use of the data to evaluate and improve satellite retrieval schemes will extend the impact of these
873 SO datasets. Nonetheless, it will be advantageous to collect future aircraft and ship-based datasets
874 over the SO. In order for future data to have the maximum impact, it could be desirable to use a
875 Lagrangian approach to aircraft data collection rather than the Eulerian approach used during
876 SOCRATES. Although the Eulerian approach was beneficial for characterizing the SO
877 environment, a Lagrangian approach would allow for better understanding of how clouds evolve
878 over longer periods of time by tracing their evolution on subsequent days. In addition, a focus on
879 the transition season where there is a greater variability in the strength of phytoplankton blooms,
880 and the winter seasons where biological activity is low would allow for testing on hypotheses
881 related to the impact of biogenic aerosol species and generally provide a more thorough
882 understanding of seasonal differences. More comprehensive measurements of aerosol chemical
883 properties as well as of cloud particles with sizes between 50 and 150 μm , perhaps through

884 holographic probes, would also be beneficial. Nevertheless, the publicly available CAPRICORN,
885 MICRE, MARCUS and SOCRATES data significantly extend the availability of data on cloud,
886 precipitation and aerosol properties over the SO, and will offer rich datasets for future studies.

887

888 **Acknowledgments**

889 This work was supported by the National Science Foundation (NSF) through grants AGS-
890 1628674 (GM) and AGS-1762096 (GM) and by the United States Department of Energy through
891 grant DE-SC0018626. PJD, TCJH, and KAM acknowledge NSF grant AGS-1660486 and DOE
892 grant DE- SC0018929. KAM acknowledges support by an NSF Graduate Research Fellowship
893 under Grant No. 006784. JU was supported by the National Research Foundation of Korea
894 (NRF) grant funded by the Korean government (MSIT) (No. 2020R1A2C1013278) and by Basic
895 Science Research Program through the NRF funded by the Ministry of Education
896 (No. 2020R1A6A1A03044834). CM was supported primarily by the National Center for
897 Atmospheric Research and received travel support from NSF AGS-1660486. The material in the
898 article is based upon work supported by the National Center for Atmospheric Research, which is
899 a major facility sponsored by the NSF under Cooperative Agreement No. 1852977. The data
900 were collected using NSF's Lower Atmosphere Observing Facilities, which are managed and
901 operated by NCAR's Earth Observing Laboratory. The efforts of the entire SOCRATES,
902 MARCUS, MICRE and CAPRICORN teams in collecting the high quality data sets are
903 appreciated. Technical, logistical and ship support for MARCUS and MICRE were provided by
904 the AAD through Australian Antarctic Science projects 4431, 4292 and 4387, and we thank
905 Steven Whiteside, Lloyd Symonds, Rick van den Enden, Peter de Vries, Chris Young, Chris
906 Richards, Terry Egan, Nick Cartwright and Ken Barrett for assistance. Logistical and financial

907 support was provided for CAPRICORN by the Australian Marine National Facility. Anne Marie
908 Rauker is acknowledged for assistance in INP data processing. Anne Perring is acknowledged
909 for the use of her WIBS-4A during CAPRICORN II. Paul Selleck is acknowledged for his work
910 with the ToF-ACSM during CAPRICORN II. Robyn Schofield also acknowledges support from
911 the Australian Research Council's DP160101598, LE150100048 and CE170100023 grants. The
912 SOCRATES Principal Investigators would like to thank the BoM Tasmanian regional Office for
913 the excellent forecast support and weather briefings provided during the field campaign (with
914 special thanks to Scott Carpentier, Michelle Hollister, Matthew Thomas and Robert Schaap). We
915 thank the Atmospheric Radiation Measurement (ARM) Program sponsored by the U.S. DOE,
916 Office of Science, Office of Biological and Environmental Research, Climate and Environmental
917 Science Division for their support. Any opinions, findings, and conclusions or recommendations
918 expressed in this material are those of the author(s) and do not necessarily reflect the views of
919 the funding agencies.

920

921 **Data Availability**

922 Copies of all Atmospheric Radiation Measurement (ARM) Program instrument-level data
923 collected during MARCUS and MICRE are permanently stored and available via the ARM data
924 archive (<https://adc.arm.gov/>). Data from AAD, BoM and CSIRO instruments deployed alongside
925 MARCUS and MICRE instrumentation are available from the Australian Antarctic Data Centre
926 following registration. Copies of non-ARM instrument-level data and derived (multi-instrument)
927 fields (such as cloud liquid water path and effective radius, precipitation particle type) will
928 eventually be available through ARM archive as a primary investigator data (PI data). As of the
929 time this article is being written, the processing of these data is not yet complete but are available
930 at https://atmos.uw.edu/~roj/nobackup/MARCUS_and_MICRE/Datasets/. The author(s) wish to
931 acknowledge the SOCRATES Project and the SOCRATES Data Archive Center at NCAR's Earth

932 Observing Laboratory, https://data.eol.ucar.edu/master_lists/generated/socrates/. The
933 CAPRICORN datasets are available on the CSIRO Data Access Portal <https://data.csiro.au/dap>.
934

935 **Appendix:**

936 A list of all the abbreviations used in the main text of the manuscript is provided here.

937 AA: RSV Aurora Australis

938 AAD: Australian Antarctic Division

939 AMF2: ARM Marine Facility 2

940 AR: Atmospheric River

941 ARM: Atmospheric Radiation Measurement

942 BL: Boundary Layer

943 BoM: Australian Bureau of Meteorology

944 CALIPSO: Cloud-Aerosol Lidar and Infrared Pathfinder Satellite Observation

945 CAPRICORN: Clouds Aerosols Precipitation Radiation and Atmospheric Composition over the
946 Southern Ocean

947 CCN: Cloud Condensation Nucleus

948 CDP: Cloud Droplet Probe

949 CERES: Clouds and the Earth's Radiant Energy System

950 CFAD: Contour Frequency by Altitude Diagram

951 CFDC: Continuous Flow Diffusion Chamber

952 CMIP5: Coupled Model Intercomparison Project Phase 5

953 CSU: Colorado State University

954 DMS: Dimethyl Sulfide

955 DOE: Department of Energy

956	DSD:	Drop Size Distribution
957	ECMWF:	European Center for Weather Forecasting
958	ERA-5	ECMWF Re-Analysis 5
959	FBAP:	Fluorescent Biological Aerosol Particle
960	FT:	Free Troposphere
961	GCM:	General Circulation Model
962	GPCP	Global Precipitation Climatology Project
963	GPM:	Global Precipitation Measurement
964	G-V:	Gulfstream-V Aircraft
965	HCR:	HIAPER W-band Cloud Radar
966	HGF:	Hygroscopic Growth Factor
967	HIAPER:	High-performance Instrumented Airborne Platform for Environmental Research
968	HSRL:	High Spectral Resolution Lidar
969	HYSPPLIT:	Hybrid Single Particle Lagrangian Integrated Trajectory Model
970	INP:	Ice Nucleating Particle
971	IS:	Ice Spectrometer
972	ITCZ:	Intertropical Convergence Zone
973	JAXA:	Japan Aerospace Exploration Agency
974	LW	Longwave
975	MARCUS	Measurements of Aerosols, Radiation and Clouds over the Southern Ocean
976	MBL:	Marine Boundary Layer
977	MICRE:	Macquarie Island Cloud Radiation Experiment
978	MNF :	Australian Marine National Facility

979	MSA:	Methanesulfonic Acid
980	Na:	Aerosol concentration
981	Nc:	Cloud droplet number concentration
982	NASA:	National Aeronautics and Space Administration
983	NCAR:	National Center for Atmospheric Research
984	NH:	Northern Hemisphere
985	NOAA:	National Oceanographic and Atmospheric Administration
986	NSF:	National Science Foundation
987	NWP:	Numerical Weather Prediction
988	PHIPS:	Particle Habit Imaging and Polar Scattering probe
989	PIP:	Precipitation Imaging Probe
990	RF:	Research Flight
991	RPF:	Recent Particle Formation
992	SLW:	Supercooled Liquid Water
993	SO:	Southern Ocean
994	SOCRATES:	Southern Ocean Cloud Radiation Aerosol Transport Experimental Study
995	SST:	Sea Surface Temperature
996	STEM:	Scanning Transmission Electron Microscopy
997	SW:	Shortwave
998	T:	Temperature
999	UHSAS:	Ultra High Sensitivity Aerosol Sampler
1000	VOC:	Volatile Organic Carbon
1001	WIBS4:	Waveband Integrated Bioaerosol Sensor 4

1002	WRF:	Weather Research and Forecasting Model
1003	2DC:	Two-Dimensional Cloud Probe
1004	2DS:	Two-Dimensional Stereo Probe
1005	λ :	Wavelength of Radiation
1006		
1007		

1008 **REFERENCES**

1009 Ahn, E., Y. Huang, T.H. Chubb, D. Baumgardner, P. Isaac, M. de Hoog, S. T. Siems, M.
1010 Manton, 2017: In situ observations of wintertime low-altitude clouds over the Southern
1011 Ocean. *Quart. J. Roy. Meteor. Soc.*, **143**, 1381–1394, <https://doi.org/10.1002/qj.3011>

1012 Andreae, M. O., W. Elbert and S. J. Demora, 1995: Biogenic sulfur emissions and aerosols over
1013 the tropical south-atlantic.3. Atmospheric dimethylsulfide, aerosols and cloud
1014 condensation nuclei. *J. Geophys. Res.* **100**, 11335–
1015 11356, <https://doi.org/10.1029/94jd02828>.

1016 Andreas, A, M Dooraghi, A Habte, M Kuchenreiter, I Reda, and M Sengupta. 2018. Solar
1017 Infrared Radiation Station (SIRS), Sky Radiation (SKYRAD), Ground Radiation
1018 (GNDRAD), and Broadband Radiometer Station (BRS) Instrument Handbook, U.S.
1019 Department of Energy. DOE/SC-ARM-TR-025.
1020 https://www.arm.gov/publications/tech_reports/handbooks/sirs_handbook.pdf

1021 Angulo-Martinez, M., S. Begueria, B. Latorre, and M. Fernandez-Raga, 2018: Comparison of
1022 precipitation measurements by OTT Parsivel and Thies LPM optical disdrometers.
1023 *Hydrol. Earth Syst. Sci.*, **22**, 2811-2837, <https://doi.org/10.5194/hess-22-2811-2018>.

1024 Atlas R. L., C. S. Bretherton and P. N. Blossey, 2020: How well do high and low resolution
1025 models represent observed boundary layer structures and low clouds over the
1026 summertime Southern Ocean? *J. Geophys. Res. (to be submitted 5/2020)*.

1027 Ayers, G. P. and Gras, J. L., 1991: Seasonal relationship between cloud condensation nuclei and
1028 aerosol methanesulfonate in marine air. *Nature*, **353**, 834–835.

1029 Bates, T. S., B. J. Huebert, J. L. Gras, F. B. Griffiths, and P. A. Durkee, 1998a: International
1030 Global Atmospheric Chemistry (IGAC) Project's First Aerosol Characterization
1031 Experiment (ACE 1): Overview. *J. Geophys. Res.*, **103**, 16297–16318,
1032 <https://doi.org/10.1029/97JD03741>.

1033 Bates, T.S., V.N. Kapustin, P.K. Quinn, D.S. Covert, D.J. Coffman, C. Mari, P.A. Durkee, W.
1034 DeBruyn, and E. Saltzman, 1998: Processes controlling the distribution of aerosol
1035 particles in the lower marine boundary layer during the First Aerosol Characterization
1036 Experiment (ACE-1). *J. Geophys. Res.*, **103**, 16369-16384,
1037 <https://doi.org/10.1029/97JD03720>.

1038 Bates, T.S., P.K. Quinn, D.S. Covert, D.J. Coffman, J.E. Johnson, and A. Wiedensohler, 2000:
1039 Aerosol physical properties and processes in the lower marine boundary layer: A
1040 comparison of shipboard sub-micron data from ACE 1 and ACE 2. *Tellus*, **52**, 258- 272,
1041 <https://doi.org/10.3402/tellusb.v52i2.16104>.

1042 Bigg, E. K., 1973: Ice nucleus concentrations in remote areas, *J. Atmos. Sci.*, **30**, 1153–1157,
1043 [https://doi.org/10.1175/1520-0469\(1973\)030<1153:INCIRA>2.0.CO;2](https://doi.org/10.1175/1520-0469(1973)030<1153:INCIRA>2.0.CO;2)

1044 Bodas-Salcedo, A., M. J. Webb, S. Bony, H. Chepfer, J. L. DuFresne, S. A. Klein, Y. Zhang, R.
1045 Marchand, J. M . Haynes, R. Pincus, and V. O. John, 2011: COSP: Satellite simulation
1046 software for model assessment. *Bull. Amer. Meteor. Soc.*, **92**, 1023-1043,
1047 <https://doi.org/10.1175/2011BAMS2856.1>

1048 Bodas-Salcedo, A., K.D. Williams, M.A. Ringer, I. Beau, J.N.S. Cole, J.-L. Dufresne, T.
1049 Koshiro, B. Stevens, Z. Wang, and T. Yokohata, 2014: Origins of the solar radiation

1050 biases over the Southern Ocean in CFMIP2 models. *J. Climate*, **27**, 41–56,
1051 <https://doi.org/10.1175/JCLI-D-13-00169.1>.

1052 Bodas-Salcedo, A., T. Andrews, A.V. Karmalkar, and M.A. Ringer, 2016: Cloud liquid water
1053 path and radiative feedbacks over the Southern Ocean. *Geophys. Res. Lett.*, **43**, 10938-
1054 10946, doi:10.1002/2016GL070770.

1055 Boers, R., J. B. Jensen, P. B. Krummel, and H. Gerber, 1996: Microphysical and short-wave
1056 radiative structure of wintertime stratocumulus clouds over the Southern Ocean. *Quart. J.*
1057 *Roy. Meteor. Soc.*, **122**, 1307–1339, <https://doi.org/10.1002/qj.49712253405>.

1058 Boers, R., J. B. Jensen, and P. B. Krummel, 1998: Microphysical and short-wave radiative
1059 structure of stratocumulus clouds over the Southern Ocean: Summer results and seasonal
1060 differences, *Quart. J. R. Meteor. Soc.*, **124**, 151–168,
1061 <https://doi.org/10.1002/qj.49712454507>.

1062 Bryan, G. H. and J.M. Fritsch, 2002: A Benchmark Simulation for Moist Nonhydrostatic
1063 Numerical Models. *Monthly Weather Review*, **130**, 2917–2928,
1064 [https://doi.org/10.1175/1520-0493\(2002\)130<2917:ABSMN>2.0.CO;2](https://doi.org/10.1175/1520-0493(2002)130<2917:ABSMN>2.0.CO;2).

1065 Burrows, S. M., C. Hoose, U. Pöschl and M.G. Lawrence, 2013: Ice nuclei in marine air:
1066 biogenic particles or dust? *Atmos. Chem. Phys.*, **13**, 245–267. <https://doi.org/10.5194/acp-13-245-2013>.

1068 Carslaw, K, A. Lee1, C. L. Reddington, K. J. Pringle, A. Rap, P. M. Forster, G. W. Mann1, D. V.
1069 Spracklen, M. T. Woodhouse, L. A. Regayre1 and J. R. Pierce, 2013: Large contribution
1070 of natural aerosols to uncertainty in indirect forcing. *Nature*, **503**, 67-71,
1071 <http://doi:10.1038/nature12674>.

1072 Carslaw, K. S., O. Boucher, D. V. Spracklen, G. W. Mann, J. G. L. Rae, S. Woodward, and M.
1073 Kulmala, 2010: A review of natural aerosol interactions and feedbacks within the Earth
1074 system. *Atmos. Chem. Phys.*, **10**, 1701–1737, <https://doi.org/10.5194/acp-10-1701-2010>

1075 Carslaw, K.S., L. A. Lee, C. L. Reddington, K. J. Pringle, A. Rap, P. M. Forster, G. W. Mann, D.
1076 V. Spracklen, M. T. Woodhouse, L. A. Regayre, and J. R. Pierce, 2013: Large
1077 contribution of natural aerosols to uncertainty in indirect forcing. *Nature*, **503**, 67-71,
1078 <https://doi.org/10.1038/nature12674>.

1079 Ceppi, P., M. D. Zelinka, and D. L. Hartmann, 2014: The response of the Southern Hemispheric
1080 eddy-driven jet to future changes in shortwave radiation in CMIP5, *Geophys. Res. Lett.*,
1081 **41**, 3244–3250, doi:10.1002/2014GL060043.

1082 Choi, Y. S., C.H. Ho, S.W. Kim, and R.S. Lindzen, 2010: Observational Diagnosis of Cloud Phase
1083 in the Winter Antarctic Atmosphere for Parameterizations in Climate Models. *Adv. Atmos.*
1084 *Sci.*, **27**, 1233-1245. doi: 10.1007/s00376-010-9175-3.

1085 Chubb, T., Y. Huang, J. Jensen, T. Campos, S. Siems, and M. Manton, 2016: Observations of
1086 high droplet number concentrations in Southern Ocean boundary layer clouds, *Atmos.*
1087 *Chem. Phys.*, **16**, 971–987, <https://doi.org/10.5194/acp-16-971-2016>.

1088 Chubb, T. H., J.B. Jensen, S.T. Siems, and M.J. Manton, 2013: In situ observations of
1089 supercooled liquid clouds over the Southern Ocean during the HIAPER Pole-to-Pole
1090 Observation campaigns, *Geophys. Res. Lett.*, **40**, 5280–5285,
1091 <https://doi.org/10.1002/grl.50986>.

1092 Clarke, A. D., 1993: Atmospheric Nuclei in The Pacific Midtroposphere - Their Nature,
1093 Concentration, and Evolution. *J. Geophys. Res.*, **98**, 20633–
1094 20647, <https://doi.org/10.1029/93jd00797>.

1095 Clarke, A. D., J.L. Varner, F. Eisele, R.L. Mauldin, D. Tanner and M. Litchy, 1998: Particle
1096 production in the remote marine atmosphere: Cloud outflow and subsidence during ACE
1097 1. *J. Geophys. Res.*, **103**, 16397-16409, <https://doi.org/10.1029/97JD02987>.

1098 Clement, C. F., I. Ford, J., Twohy, C. H., A. Weinheimer, and T. Campos, 2002: Particle
1099 production in the outflow of a midlatitude storm. *J. Geophys. Res.*, **107**, AAC 5-1-AAC
1100 5-9, <https://doi.org/10.1029/2001JD001352>.

1101 Cober, S.G., and G.A. Isaac, 2012: Characterization of aircraft icing environments with
1102 supercooled large drops for application to commercial aircraft certification. *J. Appl.*
1103 *Meteor.*, **51**, 265-284, <https://doi.org/10.1175/JAMC-D-11-022.1>.

1104 Covert, D. S., V.N. Kapustin, P.K. Quinn, and T. S. Bates, 2002: New Particle Formation in The
1105 Marine Boundary-Layer. *J. Geophys. Res.*, **97**, 20581–
1106 20589, <https://doi.org/10.1029/92jd02074>.

1107 Covert, D. S., V.N. Kapustin, T.S. Bates, and P.K. Quinn, 1996: Physical properties of marine
1108 boundary layer aerosol particles of the mid-Pacific in relation to sources and
1109 meteorological transport. *J. Geophys. Res.*, **101**, 6919-6930,
1110 <https://doi.org/10.1029/95JD03068>.

1111 D'Alessandro, J., G. McFarquhar, W. Wu, J. Stith, M. Schnaiter, and E. Jaervinen, 2020: Spatial
1112 heterogeneity of liquid, ice and mixed phase low-level clouds over the Southern Ocean
1113 derived using in situ observations acquired during SOCRATES. *J. Geophys. Res.*, In
1114 preparation.

1115 Danabasoglu, G., J.-F. Lamarque, J. Bacmeister, D. A. Bailey, A. K. DuVivier, J. Edwards, L. K.
1116 Emmons, J. Fasullo, R. Garcia, A. Gettelman, C. Hannay, M.M. Holland, W.G. Large,
1117 P.H. Lauritzen, D.M. Lawrence, J.T.M. Lenaerts, K. Lindsay, W.H. Lipscomb, M.J.
1118 Mills, R. Neale, K.W. Oleson, B. Otto-Btiesner, A.S. Phillips, W. Sacks, S. Times, L. van

1119 Kampenhout, M. Vertenstein, A. Bertini, J. Dennis, C. Deser, C. Fischer, B. Fox-
1120 Kemper, J.E. Kay, D. Kinnison, P.J. Kushner, V.E. Larson, M.C. Long, S. Mickelson,
1121 J.K. Moore, E. Nienhouse, L. Polvani, P.J. Rasch, W.G. Strand, 2020: "The Community
1122 Earth System Model Version 2 (CESM2). *Journal of Advances in Modeling Earth
1123 Systems* **12**, e2019MS001916, <https://doi.org/10.1029/2019MS001916>.

1124 Delanoë J and R. Hogan, 2010: Combined CloudSat-CALIPSO-MODIS retrievals of the
1125 properties of ice clouds. *J. Geophys. Res.*, **115**, D00H29, doi:10.1029/2009JD012346.

1126 DeMott, P.J., Hill, T.C., McCluskey, C.S., Prather, K.A., Collins, D.B., Sullivan, R.C., Ruppel,
1127 M.J., Mason, R.H., Irish, V.E., Lee, T. and Hwang, C.Y., 2015. Sea spray aerosol as a
1128 unique source of ice nucleating particles. *Proc. Nat. Acad. Sci. USA*,
1129 doi:10.1073/pnas.1514034112.

1130 FAA, 2015: Airplane and engine certification requirements in supercooled large drop, mixed
1131 phase and ice crystal icing conditions; Final rule. Parts 25 and 33, Aeronautics and Space,
1132 Title 14, U.S. Code of Federal Regulations, National Archives and Records
1133 Administration, 34 pp.

1134 Flato, G., J. Marotzke, B. Abiodun, P. Braconnot, S.C. Chou, W. Collins, P. Cox, F. Driouech, S.
1135 Emori, V. Eyring, C. Forest, P. Gleckler, E. Guilyardi, C. Jakob, V. Kattsov, C. Reason,
1136 M. Rummukainen, 2013: Evaluation of climate models. In Climate change 2013: The
1137 physical science basis. Contribution of working group I to the fifth assessment report of
1138 the intergovernmental panel on climate change. *Cambridge University Press*. 741-882,
1139 <https://doi.org/10.1017/CBO9781107415324.020>

1140 Gettelman, A., C.G. Bardeen, C.S. McCluskey, E. Jävinen, J. Stith, C.G. Bretherton, G.
1141 McFarquhar, C. Twohy, J. D'Alessandro, W. Wu, 2020: Simulating Observations of
1142 Southern Ocean Clouds and Implications for Climate. *J. Geophys. Res. (accepted)*

1143 Ghan, S. J., S. J. Smith, M. Wang, K. Zhang, K. Pringle, K. Carslaw, J. Pierce, S. Bauer, and P.
1144 Adams, 2013: A simple model of global aerosol indirect effects. *J. Geophys. Res.*, **118**,
1145 6688–6707, <https://doi.org/10.1002/jgrd.50567>.

1146 Gras, J. L., and M. Keywood, 2017: Cloud condensation nuclei over the Southern Ocean: wind
1147 dependence and seasonal cycles, *Atmos. Chem. Phys.*, **17**, 4419-4432,
1148 <https://doi.org/10.5194/acp-17-4419-2017>.

1149 Grecu, M., W.S. Olson, S.J. Munchak, S. Ringerud, L. Liao, Z. Haddad, B.L. Kelley, S.F.
1150 McLaughlin, 2016: The GPM combined algorithm. *J. Atmos. Ocean. Tech.*, **33**, 2225-
1151 2245, doi:10.1175/JTECH-D-16-0019.1.

1152 Grosvenor, D.P., and R. Wood, 2014: The effect of solar zenith angle on MODIS cloud optical
1153 and microphysical retrievals within marine liquid water clouds. *Atmos. Chem. Phys.*, **14**,
1154 7291-7321, doi:10.5194/acp-14-7291-2014.

1155 Grosvenor, D. P., Choularton, T. W., Lachlan-Cope, T., Gallagher, M. W., Crosier, J., Bower, K.
1156 N., Ladkin, R. S., and Dorsey, J. R.: In-situ aircraft observations of ice concentrations
1157 within clouds over the Antarctic Peninsula and Larsen Ice Shelf, *Atmos. Chem. Phys.*, **12**,
1158 11275–11294, doi:10.5194/acp12-11275-2012, 2012.

1159 Hande, L. B., S.T. Siems, M.J. Manton and D. Belusic, 2012: Observations of wind shear over
1160 the Southern Ocean. *J. Geophys. Res.*, **117**, D12206.

1161 <https://doi.org/10.1029/2012JD017488>.

1162 Hakim, J. R. H. G. J. (2013). *An Introduction to Dynamic Meteorology* (Fifth ed.). Academic
1163 Press: Elsevier, 552 pp.

1164 Hartery, S., D.W. Toohey, L. Revell, K. Sellegrí, P. Kuma, M. Harvey and A.J.
1165 McDonald, 2020: Constraining the surface flux of sea spray particles from the Southern
1166 Ocean. *J. Geophys. Res.*, **125**, e2019JD032026. <https://doi.org/10.1029/2019JD032026>.

1167 Hegg, D. A., R.J. Ferek, P.V. Hobbs and L.F. Radke, 1991: Dimethyl Sulfide and Cloud
1168 Condensation Nucleus Correlations in The Northeast Pacific-Ocean. *J. Geophys. Res.*, **96**,
1169 13189–13191, <https://doi.org/10.1029/91jd01309>.

1170 Heidinger, A. K., 2011: ABI cloud height. NOAA NESDIS Center for Satellite Applications and
1171 Research Algorithm Theoretical Basis Doc Ver. 3., 77 pp,
1172 https://www.star.nesdis.noaa.gov/goesr/docs/ATBD/Cloud_Height.pdf

1173 Hinkelmann, L. and R. Marchand, 2020: Evaluation of CERES and CloudSat surface radiative
1174 fluxes over the Southern Ocean, *Earth and Space Science*, **7**, e2020EA001224,
1175 <https://doi.org/10.1029/2020EA001224>.

1176 Holben, B. N., T.F. Eck, I. Slutsker, D. Tanré J.P. Buis, A. Setzer, E. Vermote, J.A. Reagan, J.
1177 Kaufman, T. Nakajima, F. Lavenu, I. Jankowiak, and A. Smirnov, 1998: AERONET – A
1178 federated instrument network and data archive for aerosol characterization, *Remote Sens.*
1179 *Environ.*, **66**, 1–16,

1180 Hoose, C., J.E. Kristjánsson, T. Iversen, A. Kirkevåg, Ø. Seland, and A. Gettelman, 2009:
1181 Constraining cloud droplet number concentration in GCMs suppresses the aerosol indirect
1182 effect, *Geophys. Res. Lett.*, **36**, L12807, <https://doi.org/10.1029/2009GL038568>

1183 Hou, A. Y., K.K. Ramesh, S. Neeck, A.A. Azarbarzin, C.D. Kummerow, M. Kojima, R. Oki, K.
1184 Nakamura, and T. Iguchi, 2014: The global precipitation measurement mission. *Bull. Amer.*
1185 *Meteor. Soc.*, **95**, 701–722, <https://doi.org/10.1175/BAMS-D-13-00164.1>.

1186 Hu, Y., S. Rodier, K. Xu, W. Sun, J. Huang, B. Lin, P. Zhai, and D. Josset, 2010: Occurrence,
1187 liquid water content, and fraction of supercooled water clouds from combined
1188 CALIOP/IIR/MODIS measurements. *J. Geophys. Res.*, **115**, D00H34,
1189 doi:10.1029/2009JD012384

1190 Huang, Y., C.N. Franklin, S.T. Siems, M.J. Manton, T. Chubb, A. Lock, S. Alexander. and A.
1191 Klekociuk, 2015: Evaluation of boundary-layer cloud forecasts over the Southern Ocean
1192 in a limited-area numerical weather prediction system using in situ , space-borne and
1193 ground-based observations. *Q.J.R. Meteorol. Soc.*, **141**, 2259-2276.
1194 <https://doi:10.1002/qj.2519>

1195 Huang, Y., S.T. Siems, M.J. Manton, L.B. Hande and J.M. Haynes, 2012a: The structure of low-
1196 altitude clouds over the Southern Ocean as seen by CloudSat. *Journal of Climate*, **25**,
1197 2535–2546. <https://doi.org/10.1175/JCLI-D-11-00131.1>

1198 Huang, Y., S.T. Siems, M.J. Manton, A. Protat and J. Delano , 2012b: A study on the low-
1199 altitude clouds over the Southern Ocean using the DARDAR-MASK. *J. Geophys. Res.*,
1200 **117**, D18204. <https://doi.org/10.1029/2012JD017800>.

1201 Huang, Y., M. Manton, S. Siems, A. Protat, L. Majewskic, and H. Nguyen (2019). Evaluating
1202 Himawari-8 Cloud Products Using Shipborne and CALIPSO Observations: Cloud-top

1203 Height and Cloud-top Temperature. *J. Atmos. Ocean. Tech.* doi: 10.1175/JTECH-D-18-
1204 0231.1.

1205 Hudson, J.G., Y. Xie, and S.S. Yum, 1998: Vertical distribution of cloud condensation nuclei
1206 spectra over the summertime Southern Ocean. *J. Geophys. Res.*, **103**, 16609-16624,
1207 doi:10.1029/97JD03438.

1208 Humphries, R. S., A. R. Klekociuk, R. Schofield, M. D. Keywood, J. Ward, and S. R. Wilson,
1209 2016: Unexpectedly high ultrafine aerosol concentrations above East Antarctic sea ice.
1210 *Atmos. Chem. Phys.* **16**, 2185–2206. <https://doi.org/10.5194/acp-16-2185-2016>

1211 Humphries, R. S., R. Schofield, M. D. Keywood, J. Ward, J. R. Pierce, C. M. Gionfriddo, M. T.
1212 Tate, D. P. Krabbenhoft, I. E. E. Galbally, S. B. B. Molloy, A. R. Klekociuk, P. V.
1213 Johnston, K. Kreher, A. J. Thomas, A. D. D. Robinson, N. R. P. Harris, R. Johnson, and
1214 S. R. Wilson, 2015: Boundary layer new particle formation over East Antarctic sea ice -
1215 possible Hg driven nucleation? *Atmos. Chem. Phys.*, **15**, 13339–13364.
1216 <https://doi.org/10.5194/acp-15-13339-2015>

1217 Hwang, Y.-T., and D.M.M. Frierson, 2013: Link between the double-Intertropical Convergence
1218 Zone problem and cloud biases over the Southern Ocean. *Proc. Natl. Acad. Sci.*, **110**, 4935-
1219 4940.

1220 IPCC, 2013: Climate Change 2013: The Physical Science Basis. Contribution of Working Group
1221 I to the Fifth Assessment Report of the Intergovernmental Panel on Climate Change
1222 [Stocker, T.F., D. Qin, G.-K. Plattner, M. Tignor, S.K. Allen, J. Boschung, A. Nauels, Y.
1223 Xia, V. Bex and P.M. Midgley (eds.)]. *Cambridge University Press*, Cambridge, United
1224 Kingdom and New York, NY, USA, 1535 pp.

1225 Kanitz, T., P. Seifert, A. Ansmann, R. Engelmann, D. Althausen, C. Casiccia, and E.G. Rohwer,
1226 2011: Contrasting the impact of aerosols at northern and southern midlatitudes on
1227 heterogeneous ice formation. *Geophy. Res. Lett.*, **38**, 5. doi: L17802

1228 Kay, J.E., C. Wall, V. Yettella, B. Medeiros, C. Hannay, P. Caldwell, and C. Bitz, 2016: Global
1229 climate impacts of fixing the Southern Ocean shortwave radiation bias in the Community
1230 Earth System Model (CESM). *J. Climate*, **29**, 4617-4636, DOI: 10.1175/JCLI-D-15-
1231 0358.1

1232 Klekociuk, A. R., W.J.R. French, S.P. Alexander, P. Kuma and A.J. McDonald, 2020: The state
1233 of the atmosphere in the 2016 southern Kerguelen Axis campaign region. *Deep Sea*
1234 *Research II*, **174**. <https://doi.org/10.1016/j.dsr2.2019.02.001>.

1235 Klekociuk, A.R., D.J. Ottaway, A.D. MacKinnon, I.M. Reid, L.V. Twigger and S.P. Alexander,
1236 2020: Australian lidar measurements of aerosol layers associated with the 2015 Calbuco
1237 eruption. *Atmosphere*, **11**, 124. <https://doi.org/10.3390/atmos11020124>

1238 Klepp, C., S. Michel, A. Protat, J. Burdanowitz, N. Albern, A. Dahl, M. Kähnert, V. Louf, S.
1239 Bakan, and S. A. Buehler, 2018: OceanRAIN, a new in-situ shipboard global ocean
1240 surface-reference dataset of all water cycle components. *Sci Data* **5**, 180122.
1241 <https://doi.org/10.1038/sdata.2018.122>

1242 Korhonen, H., K. S. Carslaw, D. V. Spracklen, G. W. Mann, and M. T. Woodhouse, 2008:
1243 Influence of oceanic dimethyl sulfide emissions on cloud condensation nuclei
1244 concentrations and seasonality over the remote Southern Hemisphere oceans: A global
1245 model study. *J. Geophys. Res.*, **113**, <https://doi.org/10.1029/2007JD009718>.

1246 Korolev, A., G. McFarquhar, P. Field, C. Franklin, P. Lawson, Z. Wang, E. Williams, S. Abel,
1247 D. Axisa, S. Borrmann, J. Crosier, J. Fugal, M. Krämer, U. Lohmann, O. Schlenczaek,
1248 and M. Wendisch, 2017: Mixed-phase clouds: progress and challenges. *Meteor. Monogr.*
1249 doi:10.1175/AMSMONOGRAPH-D-17-0001.1, **58**, 5.1-5.50.

1250 Kulmala, M., H. Vehkamäki, T. Petäjä, M. Dal Maso, A. Lauri, V.-M. Kerminen, W. Birmili and
1251 P.H. McMurry, 2004: Formation and growth rates of ultrafine atmospheric particles: a
1252 review of observations. *J. Aerosol Sci.*, **35**, 143–
1253 176, <https://doi.org/10.1016/j.jaerosci.2003.10.003>

1254 Kuma, P., A.J. McDonald, O. Morgenstern, S.P. Alexander, J.J. Cassano, S. Garrett, J. Halla, S.
1255 Hartery, M.J. Harvey, S. Parsons, G. Plank, V. Varma and J. Williams, 2020: Evaluation
1256 of Southern Ocean cloud in the HadGEM3 general circulation model and MERRA-2
1257 reanalysis using ship-based observations, *Atmos. Chem. Phys. Discuss.*, **20** (11), 6607–
1258 6630, <https://doi.org/10.5194/acp-20-6607-2020>.

1259 Lang, F., Y. Huang, S.T. Siems and M.J. Manton, 2018: Characteristics of the marine
1260 atmospheric boundary layer over the Southern Ocean in response to the synoptic forcing.
1261 *J. Geophys. Res. Atmo.*, **123**, 7799—7820. <https://doi.org/10.1029/2018JD028700>.

1262 Lim, E.-P., and I. Simmonds, 2007: Southern Hemisphere winter extratropical cyclone
1263 characteristics and vertical organization observed with the ERA-40 reanalysis data in
1264 1979-2001. *Journal of Climate*, **20**, 2675-2690. <https://doi.org/10.1175/JCLI4135.1>

1265 Mace, G. G., and A. Protat, 2018: Clouds over the Southern Ocean as observed from the RV
1266 Investigator during CAPRICORN. Part 2: The properties of non-precipitating
1267 stratocumulus. *J. Appl. Meteor. Clim.*, **57**, 1805-1823. <https://doi.org/10.1175/JAMC-D-17-0195.1>

1269 Mace, G. G., Q. Zhang, M. Vaughan, R. Marchand, G. Stephens, C. Trepte, and D. Winker,
1270 2009: A description of hydrometeor layer occurrence statistics derived from the first year
1271 of merged Cloudsat and CALIPSO data. *J. Geophys. Res.*, **114**, D00A26.

1272 <https://doi.org/10.1029/2007JD009755>

1273 Mace, G. G., and Q. Zhang, 2014: The CloudSat radar-lidar geometrical profile product (RL-
1274 GeoProf): Updates, improvements, and selected results. *J. Geophys. Res. Atmos.*, **119**,
1275 9441–9462. <https://doi:10.1002/2013JD021374>.

1276 Marchand, R., R. Wood, C. Bretherton, G. McFarquhar, A. Protat, P. Quinn, S. Siems, C. Jakob,
1277 S. Alexander, and B. Weller, 2014: The Southern Ocean Clouds, Radiation Aerosol
1278 Transport Experimental Study (SOCRATES). whitepaper available from
1279 https://atmos.uw.edu/~roj/nobackup/Southern_Ocean_Workshop_2014/Southern_Ocean_
1280 Workshop_2014_White_Paper.pdf.

1281 McCoy, D. T., S. M. Burrows, R. Wood, D. P. Grosvenor, S. M. Elliott, P. L. Ma, P. J. Rasch, and
1282 D. L. Hartmann, 2015a: Natural aerosols explain seasonal and spatial patterns of Southern
1283 Ocean cloud albedo. *Sci. Adv.*, **1**, p.e1500157. <https://doi.org/10.1126/sciadv.1500157>

1284 McCluskey, C. S., T.C.J. Hill, C. Sultana, O. Laskina, J. Trueblood, M.V. Santander, C.M.
1285 Beall, J.M. Michaud, S.M. Kreidenweis, K.A. Prather, V. Grassian, P.J. DeMott, 2018a:
1286 A Mesocosm Double Feature: Insights into the Chemical Makeup of Marine Ice
1287 Nucleating Particles, *J Atmos Sci*, **75**, 2405-2423. <https://doi.org/10.1175/JAS-D-17->
1288 [0155.1](https://doi.org/10.1175/JAS-D-17-0155.1)

1289 McCluskey, C. S., T. C. J. Hill, R. S. Humphries, A. M. Rauker, A. M., S. Moreau, S., P. G.
1290 Strutton, S. D. Chambers, A. G. Williams, I. McRobert , J. Ward, M. D. Keywood, J.
1291 Harnwell, W. Ponsonby, Z.M. Loh , P. B. Krummel, A. Protat, S.M. Kreidenweis, and

1292 P. J. DeMott, 2018b: Observations of ice nucleating particles over Southern Ocean
1293 waters. *Geophysical Research Letters*, **45**, 11,989–11,997. <https://doi.org/10.1029/2018GL079981>.

1294

1295 McCluskey, C. S., J. Ovadnevaite, M. Rinaldi, J. Atkinson, F. Belosi, D. Ceburnis, S. Marullo, T.
1296 C. J. Hill, U. Lohmann, Z. A. Kanji, C. O'Dowd, S. M. Kreidenweis¹, P. J. DeMott,
1297 2018c: Marine and terrestrial organic ice nucleating particles in pristine marine to
1298 continentally-influenced northeast Atlantic air masses. *J. Geophys. Res.*, **123**, 6196–
1299 6212. <https://doi.org/10.1029/2017JD028033>.

1300 McCluskey, C. S., P. J. DeMott, P.-L. Ma, and S. M. Burrows, 2019: Numerical representations
1301 of marine ice-nucleating particles in remote marine environments evaluated against
1302 observations. *Geophysical Research Letters*, **46**, 7838–7847. <https://doi.org/10.1029/2018GL081861>.

1303

1304 McCoy, D. T., S. M. Burrows, R. Wood, D. P. Grosvenor, S. M. Elliott, P. L. Ma, P. J. Rasch, and
1305 D. L. Hartmann, 2015a: Natural aerosols explain seasonal and spatial patterns of Southern
1306 Ocean cloud albedo. *Sci. Adv.*, **1**(6), p.e1500157.

1307 McCoy, D. T., D. L. Hartmann, M. D. Zelinka, P. Cessi, and D. P. Grosvenor, 2015b: Mixed-
1308 phase cloud physics and Southern Ocean cloud feedback in climate models. *J. Geophys.
1309 Res.*, **120**(18), 9539-9554.

1310 McCoy, I. L., Bretherton, C. S., Wood, R., Twohy, C. H., Gettleman, A. Bardeen, C., 2020:
1311 Recent particle formation and aerosol variability near Southern Ocean low clouds. *in
1312 prep*

1313 McFarquhar, G.M., S. Ghan, J. Verlinde, A. Korolev, J. W. Strapp, B. Schmid, J. M. Tomlinson,
1314 M. Wolde, S. D. Brooks, D. Cziczo, M. K. Dubey, J. Fan, C. Flynn, I. Gultepe, J. Hubbe,

1315 M. K. Gilles, A. Laskin, P. Lawson, W. R. Leaitch, P. Liu, X. Liu, D. Lubin, C.
1316 Mazzoleni, A.-M. Macdonald, R. C. Moffet, H. Morrison, M. Ovchinnikov, M. D. Shupe,
1317 D. D. Turner, S. Xie, A. Zelenyuk, K. Bae, M. Freer, and A. Glen, 2011: Indirect and
1318 Semi-Direct Aerosol Campaign (ISDAC): The impact of arctic aerosols on clouds, *Bull.*
1319 *Amer. Meteor. Soc.*, **92**, 183-201.

1320 McFarquhar, G. M., J.A. Finlon, D.M. Stechman, W. Wu, R.C. Jackson and M. Freer, 2018:
1321 University of Illinois/Oklahoma Optical Array Probe (OAP) Processing Software,
1322 <https://doi.org/10.5281/zenodo.1285969>, 2018.

1323 McInnes, L. M., D. Covert, P. K. Quinn, and M. S. Germani, 1994: Measurements of chloride
1324 depletion and sulfur enrichment in individual sea-salt particles collected from the remote
1325 marine boundary layer, *J. Geophys. Res.*, **99**, 8257-8268.
1326 <https://doi.org/10.1029/93JD03453>

1327 Morrison, A. E., S. T. Siems, and M. J. Manton, 2010: A modeling case study of mixed phase
1328 clouds over the Southern Ocean and Tasmania. *Mon. Wea. Rev.*, **138**, 839–862.
1329 <https://doi.org/10.1175/2009MWR3011.1>.

1330 Morrison, A. E., S. T. Siems, and M. J. Manton, 2011: A three-year climatology of cloud-top phase
1331 over the Southern Ocean and North Pacific. *J. Climate*, **24**, 2405–2418.

1332 Morrison, H., J. A. Curry, and V. I. Khvorostyanov, 2005: A new double-moment microphysics
1333 parameterization for application in cloud and climate models. Part I: Description. *J.*
1334 *Atmos. Sci.*, **62**, 1665-1677. <https://doi.org/10.1175/JAS3446.1>.

1335 Noh, Y.-J., Miller, S. D., Heidinger, A. K., Mace, G. G., Protat, A., & Alexander, S. P. (2019).
1336 Satellite-based detection of daytime supercooled liquid-topped mixed-phase clouds over

1337 the Southern Ocean using the Advanced Himawari Imager. *Journal of Geophysical*
1338 *Research: Atmospheres*, **124**, 2677–2701. <https://doi.org/10.1029/2018JD029524>.

1339 Pavolonis, M. J., 2010: GOES-R Advanced Baseline Imager (ABI) algorithm theoretical basis
1340 document for cloud type and cloud phase, version 2.0. NOAA NESDIS Center for
1341 Satellite Applications and Research Algorithm Theoretical Basis Doc., 86 pp.,
1342 https://www.star.nesdis.noaa.gov/goesr/docs/ATBD/Cloud_Phase.pdf.

1343 Pirjola, L., C.D. O'Dowd, I.M Brooks and M. Kulmala, 2000: Can new particle formation occur
1344 in the clean marine boundary layer? *J. Geophys. Res.*, **105**, 26531–
1345 26546. <https://doi.org/10.1029/2000jd900310>

1346 Platnick, S., and S. Twomey, 1994: Determining the susceptibility of cloud albedo to changes in
1347 droplet concentration with the advanced very high resolution radiometer, *J. Appl.*
1348 *Meteorol.*, **33**, 334-347. [https://doi.org/10.1175/1520-0450\(1994\)033<0334:DTSOCA>2.0.CO;2](https://doi.org/10.1175/1520-0450(1994)033<0334:DTSOCA>2.0.CO;2)

1349 Plummer, D.M., G.M. McFarquhar, R.M. Rauber, B.F. Jewett, and D. Leon, 2014: Structure and
1350 statistical analysis of the microphysical properties of generating cells in the comma-head
1351 region of continental winter cyclones. *J. Atmos. Sci.*, **71**, 4181-4203.

1352 Protat, A., C. Klepp, V. Louf, W. Petersen, S. P. Alexander, A. Barros, and G. G. Mace, 2019:
1353 The latitudinal variability of oceanic rainfall properties and its implication for satellite
1354 retrievals. Part 1: The latitudinal variability of drop size distribution properties. *J.*
1355 *Geophys. Res. Atmos.*, **124**, 13291-13311. <https://doi.org/10.1029/2019JD031010>.

1356 Protat, A., C. Klepp, V. Louf, W. Petersen, S. P. Alexander, A. Barros, and G. G. Mace, 2019:
1357 The latitudinal variability of oceanic rainfall properties and its implication for satellite
1358 retrievals. Part 2: The relationships between radar observables and drop size distribution
1359

1360 parameters. *J. Geophys. Res.*, **124**, 13312-13324.

1361 <https://doi.org/10.1029/2019JD031011>.

1362 Protat, A., E. Schulz, L. Rikus, Z. Sun, and Y. Xiao, 2017: Shipborne observations of the
1363 radiative effect of Southern Ocean clouds. *J. Geophys. Res.*, **122**, 318-328.

1364 <https://doi.org/10.1002/2016JD026061>

1365 Protat, A., S. A. Young, L. Rikus, and M. Whimpey, 2014: Evaluation of the hydrometeor
1366 frequency of occurrence in a limited-area numerical weather prediction system using near
1367 real-time CloudSat-CALIPSO observations. *Quart. J. Roy. Meteor. Soc.*, **140**, 2430-2443.

1368 <https://doi.org/10.1002/qj.2308>

1369 Puri, K., G. Dietachmayer, P. Steinle, M. Dix, L. Rikus, I. Logan, M. Naughton, C. Tingwell, Y.
1370 Xiao, V. Barras, I. Bermous, R. Bowen, L. Deschamps, C. Franklin, J. Fraser, T.
1371 Glowacki, B. Harris, J. Lee, T. Le, G. Roff, A. Sulaiman, H. Sims, X. Sun, Z Sun, H.
1372 Zhu, M. Chattopadhyay, and C. Engel, 2013: Implementation of the initial ACCESS
1373 numerical weather prediction system. *Aust. Meteorol. Oceanogr. J.*, **63**, 265–284.

1374 Quinn, P.K. and T.S. Bates, 2011: The case against climate regulation via oceanic phytoplankton
1375 sulfur emissions, *Nature*, **480**, 51 – 56. <https://doi.org/10.1038/nature10580>

1376 Quinn, P. K., T.S. Bates, K. Schulz, D. Coffman, A.A. Frossard, L.M. Russell, W.C. Keene, D.
1377 Kieber, 2014: Contribution of sea surface carbon pool to organic matter enrichment in
1378 sea spray aerosol. *Nat. Geosci.* **7**, 228–232. <https://doi.org/10.1038/ngeo2092>.

1379 Quinn, P., D.J. Coffman, J.E. Johnson, L.M. Upchurch and T.S. Bates, 2017: Small fraction of
1380 marine cloud condensation nuclei made up of sea spray aerosol, *Nature Geoscience*, **10**,
1381 674-679. <https://doi.org/10.1038/ngeo3003>

1382 Read, K. A., A.C. Lewis, S. Bauguitte, A.M. Rankin, R.A. Salmon, E.W. Wolff, A. Saiz-Lopez,
1383 W.J. Bloss, D.E. Heard, J.D. Lee and J.M.C. Plane, DMS and MSA measurements in the
1384 Antarctic Boundary Layer: impact of BrO on MSA production, *Atmos. Chem. Phys.*, **8**,
1385 2985-2997. <https://doi.org/10.5194/acp-8-2985-2008>

1386 Rinaldi, M., S. Decesari, E. Finessi, L. Giulianelli, C. Carbone, S. Fuzzi, C. O'Dowd, D.
1387 Ceburnis, and M.C. Facchini, Primary and secondary organic marine aerosol and oceanic
1388 biological activity: Recent results and new perspectives for future studies. *Advances in*
1389 *Meteorology*, <https://doi.org/10.1155/2010/310682>

1390 Rolph, G., A. Stein, and B. Stunder, 2017: Real-time Environmental Applications and Display
1391 sYstem: READY. Environmental modelling and software, **95**, 210-228.
1392 <https://doi.org/10.1016/j.envsoft.2017.06.025>

1393 Russell L.M., D.H. Lenschow, K.K. Laursen, P.B. Krummel, S.T. Siems, A.R. Bandy, D.C.
1394 Thornton, and T.S. Bates, 1998: Bidirectional mixing in an ACE 1 marine boundary
1395 layer overlain by a second turbulent layer. *J. Geophy. Res.*, **103**, 16,411-16,432.
1396 <https://doi.org/10.1029/97JD03437>

1397 Sanchez, K. J., C.-L. Chen, L.M. Russell, R. Betha, J. Liu, D.J. Price, P. Massoli, L.D. Ziembka,
1398 E.C. Crosbie, R.H. Moore, M. Müller, S.A. Schiller, A. Wisthaler, A.K.Y. Lee, P.K.
1399 Quinn, T.S. Bates, J. Porter, T.G. Bell, E.S. Saltzman, R.D. Vaillancourt and M.J.
1400 Behrenfeld, 2018: Substantial seasonal contribution of observed biogenic sulfate
1401 particles to cloud condensation nuclei. *Scientific Reports*, **8**, 3235.
1402 <https://doi.org/10.1038/s41598-018-21590-9>

1403 Sanchez, K. J., G.C. Roberts, G. Saliba, L.M. Russell, C. Twohy, M.J. Reeves, R.S. Humphries,
1404 M.D. Keywood, J.P. Ward, and I.M. McRobert, 2020: Cloud processes and the transport

1405 of biological emissions regulate Southern Ocean particle and cloud condensation nuclei
1406 concentrations, *Atmos. Chem. Phys. Discuss.*, <https://doi.org/10.5194/acp-2020-731>.

1407 Sato, K., J. Inoue, S.P. Alexander, G. McFarquhar, Y. Yamazaki, 2018: Improved reanalysis and
1408 prediction of atmospheric fields over the Southern Ocean using campaign-based
1409 radiosonde observations, *Geophys. Res. Lett.*, **45**, 11406 – 11413,
1410 <https://doi.org/10.1029/2018GL079037>.

1411 Schmale, J., A. Baccarini, I. Thurnherr, S. Henning, A. Efraim, L. Regayre, C. Bolas, M.
1412 Hartmann, A. Welti, K. Lehtipalo, F. Aemisegger, C. Tatzelt, S. Landwehr, R.L. Modini,
1413 F. Tummon, J.S. Johnson, N. Harris, M. Schnaiter, A. Toffoli, M. Derkani, N.
1414 Bukowiecki, F. Stratmann, J. Dommen, U. Baltensperger, H. Wernli, D. Rosenfeld, M.
1415 Gysel-Beer, and K.S. Carslaw, 2019: Overview of the Antarctic circumnavigation
1416 expedition: Study of preindustrial-like aerosols and their climate effects (ACE-SPACE).
1417 *Bull. Amer. Meteor. Soc.*, **100**, 2261-2283. <https://doi.org/10.1175/BAMS-D-18-0187.1>

1418 Sciare, J., O. Favez, R. Sarda-Este`ve, K. Oikonomou, H. Cachier, and V. Kazan, 2009: Long-
1419 term observations of carbonaceous aerosols in the Austral Ocean atmosphere: Evidence
1420 of a biogenic marine organic source, *J. Geophys. Res.*, **114**, D15302.
1421 <https://doi.org/10.1029/2009JD011998>

1422 Scott, E. L., 2019: *The Influence of Primary Nucleation and Rime Splintering on Ice Number
1423 Concentrations in Southern Ocean Cumuli*. M.S. Thesis, University of Illinois, 104 pp.

1424 Shupe, M. D., 2007: A ground-based multisensor cloud phase classifier. *J. Geophys. Res.*, **34**,
1425 L22809, <https://doi.org/10.1029/2007GL031008>

1426 Skamarock, W. C., J. B. Klemp, J. Dudhia, D. O. Gill, D. M. Barker, W. Wang, and J. G. Powers,
1427 2005: A description of the Advanced Research WRF version 2. NCAR Tech. Note
1428 NCAR/TN-468+STR, 88 pp.

1429 Skofronick-Jackson G, W.A. Petersen, W. Berg, C. Kidd, E.F. Stocker, D.B. Kirschbaum, R.
1430 Kakar, S.A. Braun, G.J. Huffman, T. Iguchi, P.E. Kirtsteller, C. Kummerow, R. Meneghini,
1431 R. Oki, W.S. Olson, Y.N. Takayabu, K. Kurukawa, and T. Wilheit, 2017: The Global
1432 Precipitation Measurement (GPM) Mission for Science and Society. *Bull. Amer. Meteor.*
1433 *Soc.*, DOI: 10.1175/BAMS-D-15-00306.1

1434 Stein, A.F., Draxler, R.R, Rolph, G.D., Stunder, B.J.B., Cohen, M.D., and Ngan, F., 2015: NOAA's
1435 HYSPLIT atmospheric transport and dispersion modeling system, *Bull. Amer. Meteor.*
1436 *Soc.*, **96**, 2059-2077, <http://dx.doi.org/10.1175/BAMS-D-14-00110.1> □

1437 Stephens, B., M. Long, R. Keeling, E. Kort, C. Sweeney, E. Apel, E. Atlas, S. Beaton, J. Bent, N. Blake, J.
1438 Bresch, J. Casey, B. Daube, M. Diao, E. Diaz, H. Dierssen, V. Donets, B. Gao, M. Gierach, R.
1439 Green, J. Haag, M. Hayman, A. Hills, H. Hoecker-Martinez, S. Honomichl, R. Hornbrook, J.
1440 Jensen, R. Li, I. McCubbin, K. McKain, E. Morgan, S. Nolte, J. Powers, B. Rainwater, K.
1441 Randolph, M. Reeves, S. Schauffler, M. Smith, K. Smith, J. Stith, G. Stossmeister, D. Toohey, and
1442 A. Watt, 2018: The O₂/N₂ ratio and CO₂ Airborne Southern Ocean (ORCAS) Study. *Bull. Amer.*
1443 *Meteor. Soc.*, doi:10.1175/BAMS-D-16-0206.1, **99**, 381-402.

1444 Stevens, B., F. Ament, S. Bony, S. Crewell, F. Ewald, S. Gross, A. Hansen, L. Hirsch, M. Jacob,
1445 T. Kölling, H. Konow, B. Mayer, M. Wendisch, M. Wirth, K. Wolf, S. Bakan, M. Bauer-
1446 Pfundstein, M. Brueck, J. Delanoë, A. Ehrlich, D. Farrell, M. Forde, F. Gödde, H. Grob,
1447 M. Hagen, E. Jäkel, F. Jansen, C. Klepp, M. Klingebiel, M. Mech, G. Peters, M. Rapp,
1448 A.A. Wing, and T. Zinner, 2019: A high-altitude long-range aircraft configured as a

1449 cloud observatory: The NARVAL Expeditions. *Bull. Amer. Meteor. Soc.*, **100**, 1061–
1450 1077, <https://doi.org/10.1175/BAMS-D-18-0198.1>

1451 Tan, I., T. Storelvmo, and M. D. Zelinka, 2016: Observational constraints on mixed-phase
1452 clouds imply higher climate sensitivity, *Science*, **352**, 224–227.

1453 <https://doi.org/10.1126/science.aad5300>

1454 Trenberth, K. E., and J.T. Fasullo, 2010: Simulation of present-day and twenty-first-century
1455 energy budgets of the southern oceans. *Journal of Climate*, **23**, 440–454.

1456 <https://doi.org/10.1175/2009JCLI3152.1>

1457 Truong, S.C.H., Y. Huang, F. Lang, M. Messmer, I. Simmonds, S.T. Siems, and M.J. Manton,
1458 2020: A climatology of the marine atmospheric boundary layer over the Southern Ocean
1459 from four field campaigns. *J. Geophys. Res. Atmo.*, Submitted.

1460 Toprak, E. and M. Schnaiter, 2013: Fluorescent biological aerosol particles measured with the
1461 Waveband Integrated Bioaerosol Sensor WIBS-4: Laboratory tests combined with a one
1462 year field study, *Atmos. Chem. Phys.*, **13**, 225–243. <https://doi.org/10.5194/acp-13-225-2013>

1463

1464 Twohy, C., and J. Anderson, 2008: Droplet nuclei in non-precipitating clouds: Composition and
1465 size matter. *Environmental Research Letters*, **3**, 045002. <https://doi.org/10.1088/1748-9326/3/4/045002>

1466

1467 Twohy, C. H., P. J. DeMott, L. M. Russell, D. W. Toohey, B. Rainwater, R. Geiss, K. J.
1468 Sanchez, S. Lewis, G. Roberts, R.S. Humphries, C. McCluskey, K. Moore, P. W. Selleck,
1469 M. D. Keywood, J. P Ward, and I.M. McRobert, 2020: Cloud-nucleating particles over
1470 the Southern Ocean in a changing climate. (submitted to ACPD).

1471 UCAR/NCAR- Earth Observing Laboratory (EOL), 1995-present: EOL Field Catalog.

1472 <https://doi.org/10.5065/D6SQ8XFB>.

1473 Uetake, J., T. C. J. Hill, K. A. Moore, P. J. DeMott, A. Protat, and S. M. Kreidenweis, 2020:

1474 Airborne bacteria confirm the pristine nature of the Southern Ocean boundary layer,

1475 *Proceedings of the National Academy of Sciences*, doi:10.1073/pnas2000134117.

1476 Vallina, S. M., R. Simó, and S. Gassó, 2006: What controls CCN seasonality in the Southern

1477 Ocean? A statistical analysis based on satellite-derived chlorophyll and CCN and model-
1478 estimated OH radical and rainfall, *Global Biogeochemical Cycles*, **20**,

1479 <https://doi.org/10.1029/2005GB002597>.

1480 Veli-Matti, K, Chen X., Vakkari V., Petaja T., Kumala M., and Bianchi F., 2018: Atmospheric

1481 new particle formation and growth: review of field observations. *Environ. Res. Lett.* **13**

1482 103003. <https://doi.org/10.1088/1748-9326/aadf3c>

1483 Vergara-Temprado, J., A. K. Miltenberger, K. Furtado, D. P. Grosvenor, B. J. Shipway, A. A.

1484 Hill, J. M. Wilkinson, P. R. Field, B. J. Murray, and K. S. Carslaw, 2018: Strong control

1485 of Southern Ocean cloud reflectivity by ice-nucleating particles. *Proceeding of the*

1486 *National Academy of Sciences*, **115**, 2687-2692.

1487 <https://doi.org/10.1073/pnas.1721627115>.

1488 Vignon, É., Alexander, S. P., DeMott, P. J., Sotiropoulou, G., Gerber, F., Hill, T. C. J.,

1489 Marchand, R., Nenes, A., Berne, A. (2020), 'Measured ice nucleating particle

1490 concentrations improve the simulation of mid-level mixed-phase clouds over the high-
1491 latitude Southern Ocean', *Journal of Geophysical Research*, submitted

1492 Waitz, F., M. Schnaiter, T. Leisner, and E. Järvinen, 2020: PHIPS-HALO: the airborne particle

1493 habit imaging and polar scattering probe - Part 3: Single particle phase discrimination and

1494 particle size distributions based on angular scattering function. *Atmos. Meas. Tech.*, In
1495 preparation.

1496 Wang, Z., S.T. Siems, D. Belusic, M.J. Manton and Y. Huang, 2015: A climatology of the
1497 precipitation over the Southern Ocean as observed at Macquarie Island. *Journal of*
1498 *Applied Meteorology and Climatology*, **54**, 2321–2337. <https://doi.org/10.1175/JAMC-D-14-0211.1>.

1500 Wang, Y., G.M. McFarquhar, R.M. Rauber, C. Zhao, W. Wu, D.M. Stechman, J.A. Finlon, J. Stith,
1501 M. Schnaiter, E. Järvinen, J. Jensen, J. Vivekanandan, and M. Dixon, 2019: Microphysical
1502 properties of generating cells over the Southern Ocean: Results from SOCRATES. *J. Geophys. Res.*, **125**, e2019JD032237.

1503 Warren, D.R., and J.H. Seinfeld, 1985: Prediction of aerosol concentrations from a burst of
1504 nucleation. *J. Colloid Interface Sci.*, **105**, 136-142.

1505 Weber, R.J., P.H. McMurry, L. Mauldin, D.J. Tanner, F.L. Eisele, F.J. Brethel, S.M. Kreidenweis, G.L.
1506 Kok, R.D. Schillawski, and D. Baumgardner, 1998: A study of new particle formation and growth
1507 involving biogenic and trace gas species measured during ACE 1. *J. Geophys. Res.*, **103**, 16385-
1508 16396.

1509 Welti, A., E. K. Bigg, P. J. DeMott, X. Gong, M. Hartmann, M. Harvey, S. Henning, P. Herenz,
1510 T. C. J. Hill, B. Hornblow, C. Leck, M. Löffler, C. S. McCluskey, A. M. Rauker, J.
1511 Schmale, C. Tatzelt, M. van Pinxteren, and F. Stratmann, 2020: Ship-based
1512 measurements of ice nuclei concentrations over the Arctic, Atlantic and Southern Ocean,
1513 in preparation for submission to *Atmos. Chem. Phys.*

1514 Wofsy, S. C., the HIPPO Science Team, and Cooperating Modeling and Satellite Teams, 2011: HIAPER
1515 Pole-to-Pole Observations (HIPPO): fine-grained, global-scale measurements of climatically

1517 important atmospheric gases and aerosols. *Phil. Trans. Roy. Soc. A*, **369**, 2073-2086,
1518 doi:10.1098/rsta.2010.0313.

1519 Wolters, E.L.A., H.M. Deneke, B.J.J.M. van den Hurk, J.F. Merink, and R.A. Roebeling, 2010: Broken and
1520 inhomogeneous cloud impact on satellite cloud particle effective radius and cloud-phase retrievals.
1521 *J. Geophys. Res.*, **115**, D10214, <https://doi.org/10.1029/2009JD012205>.

1522 Wu, C., X. Liu, M. Diao, K. Zhang, A. Gettelman, Z. Lu, J.E. Penner and Z. Lin, 2017: Direct
1523 comparisons of ice cloud macro- and microphysical properties simulated by the
1524 Community Atmosphere Model version 5 with HIPPO aircraft observations, *Atmos.*
1525 *Chem. Phys.*, **17**, 4731-4749, <https://doi.org/10.5194/acp-17-4731-2017>.

1526 Zeng, S., C. Cornet, F. Parol J. Riedi, and F. Thieuleux, 2012: A better understanding of cloud optical
1527 thickness derived from the passive sensors MODIS/AQUA and POLDER/PARASOL in the A-
1528 Train constellation. *Atmos. Chem. Phys.*, **12**, 11245-11259., doi:10.5194/acp-12-11245-2012 et al.
1529 2012

1530 Zhang, X. L., P. Massoli, P.K. Quinn, T.S. Bates and C.D. Cappa, 2014: Hygroscopic growth of
1531 submicron and supermicron aerosols in the marine boundary layer. *J. Geophys.*
1532 *Res.*, **119**, 8384-8399. <https://doi.org/10.1002/2013jd021213>

1533 Zhao, M., J.-C. Golaz, I.M. Held, H. Guo, V. Balaji, R. Benson, J.-H. Chen, X. Chen, L.J.
1534 Donner, J.P. Dunne, K. Dunne, J. Durachta, S.-M. Fan, S.M. Freidenreich, S.T. Garner,
1535 P. Ginoux, L.M. Harris, L.W. Horowitz, J.P. Krasting, A.R. Langenhorst, Z. Liang, P.
1536 Lin, S.-J. Lin, S.L. Malyshev, E. Mason, P.C.D. Milly, Y. Ming, V. Naik, F. Paulot, D.
1537 Paynter, P. Phillips, A. Radhakrishnan, V. Ramaswamy, T. Robinson, D. Schwarzkopf,
1538 C.J. Seman, E. Shevliakova, Z. Shen, H. SHin, L.G. Silvers, J.R. Wilson, M. Winton,
1539 A.T. Wittenberg, B. Wyman, B. Xiang, 2018: The GFDL Global Atmosphere and Land

1540 Model AM4.0/LM4.0: Simulation characteristics with prescribed SSTs. *J. Adv. Modeling*
1541 *Earth Sys.*, **10**, 691-734, <https://doi.org/10.1002/2017MS001208>.

1542 Zhou, X., R. Atlas, I. McCoy, C. S. Bretherton, C. Bardeen, A. Gettelman, P. Lin, and Y. Ming,
1543 2020: Evaluation of cloud and precipitation simulations in CAM6 and AM4 using
1544 observations over the Southern Ocean. *Earth Space Sci.*, submitted 4/2020. ESSO
1545 preprint: doi:10.1002/essoar.10502913.1

1546

1547

1548

1549

1550

1551

1552

1553

1554

1555

1556 **Tables**

1557 Table 1: Previous field campaigns and data collection activities over the SO

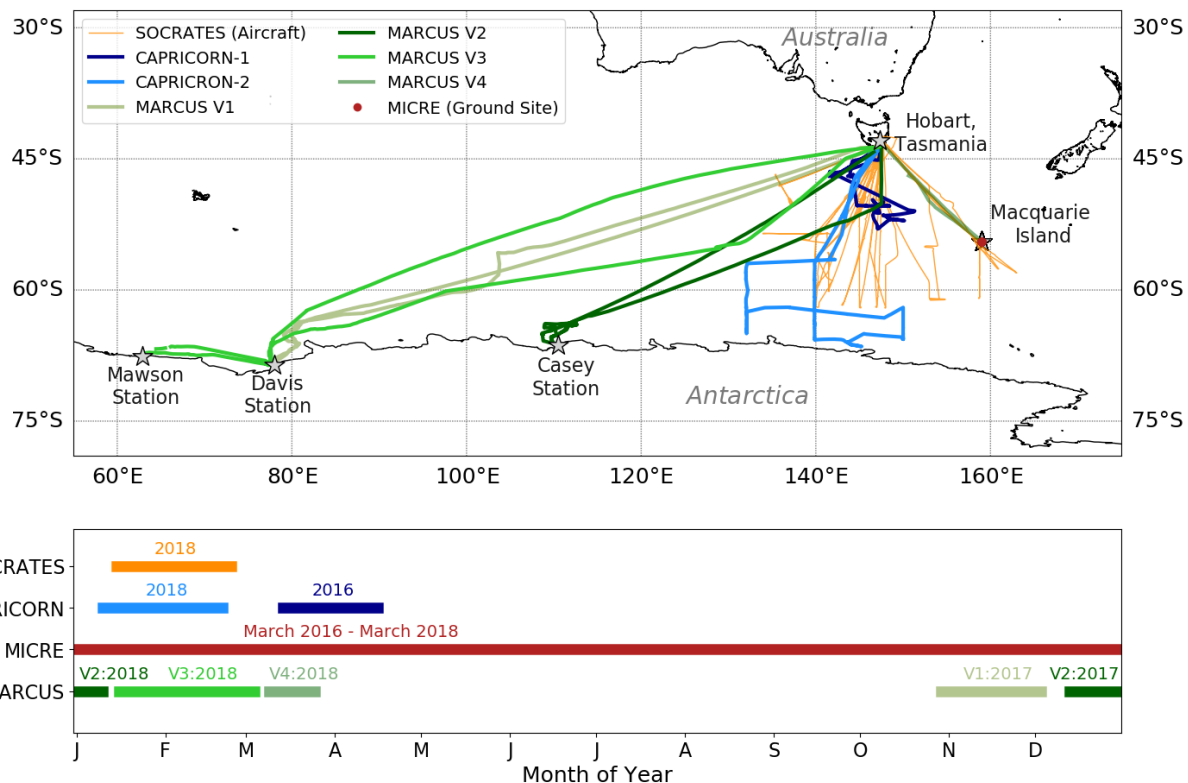
1558

Campaign	Description	Reference
Aerosol Characterization Experiment-1 (ACE-1)	sea-spray aerosol, vertical aerosol profiles and fluxes	Bates et al. 1998a, b; Clarke et al. 1998; Weber et al. 1998; Russell et al. 1998
HIAPER Pole-to-Pole Observations (HIPPO)	4 transects sampling clouds and aerosols south of Macquarie Island	Wofsy et al. 2011; Chubb et al. 2013, 2016
SIPEX II	aerosol number concentrations across polar front	Humphries 2015, 2016
O ₂ /N ₂ Ratio and CO ₂ Airborne Southern Ocean Study (ORCAS)	limited cloud sampling	Stephens et al. 2018; D'Alessandro et al. 2019
Observations near Tasmania	observations in wintertime low-altitude clouds over open ocean near Tasmania	Ahn et al. 2017; Huang et al. 2017
Cape Grim observations	CCN observations at Cape Grim (41°S, 145°E)	Gras et al. 2017
Southern Ocean Cloud Experiment (SOCEX)	aerosol optical depth and composition, clouds	Sciare et al. 2009; Boers et al. 1996, 1998
Recent ship-based observations (separate from campaigns described here)	limited set of cloud radiation and aerosol properties south of 60°S and circumpolar quantification of aerosol properties	Kuma et al. 2020; Klekociuk et al. 2020; Hartery et al. 2020; Schmale et al. 2020

1559

1560

1561 **Figures**



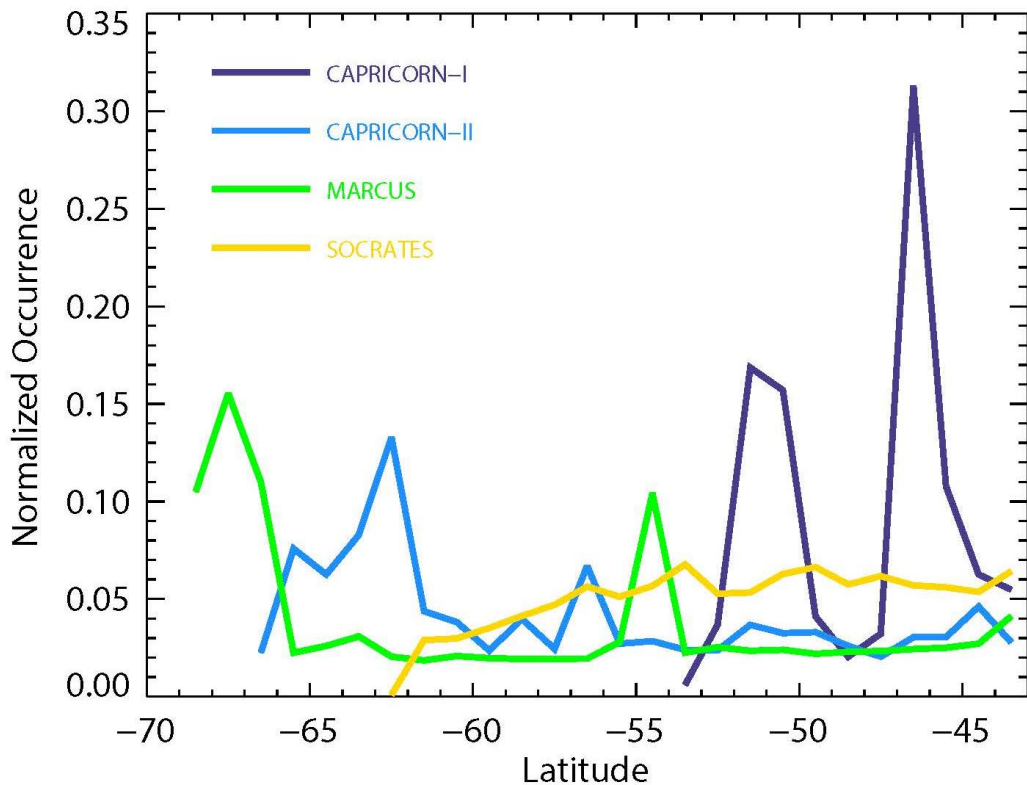
1562

1563

1564 Figure 1: Ship tracks from CAPRICORN I (dark blue), II (light blue) and MARCUS voyages

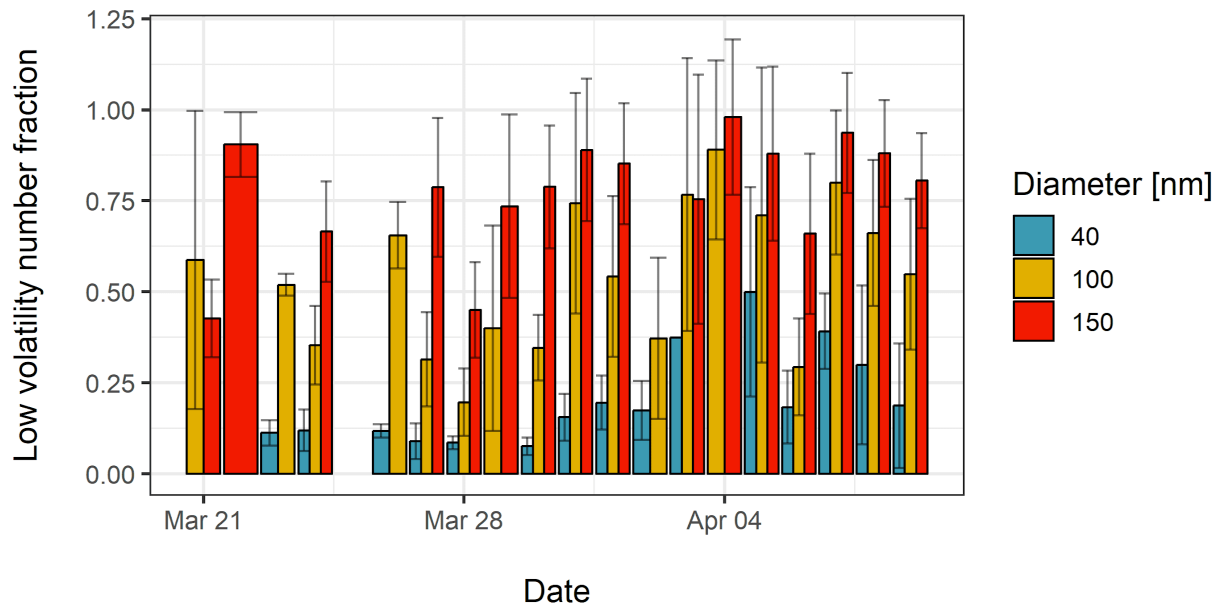
1565 (green colors), as well as the SOCERATES G-V flight tracks (orange) and the location of the
 1566 ground-observing site at Macquarie Island during MICRE (red). The locations of Mawson,
 1567 Davis, and Casey stations are also shown (grey stars). The lower panel depicts the years and
 1568 seasons corresponding to each campaign.

1569



1570
1571
1572
1573
1574
1575
1576
1577
1578

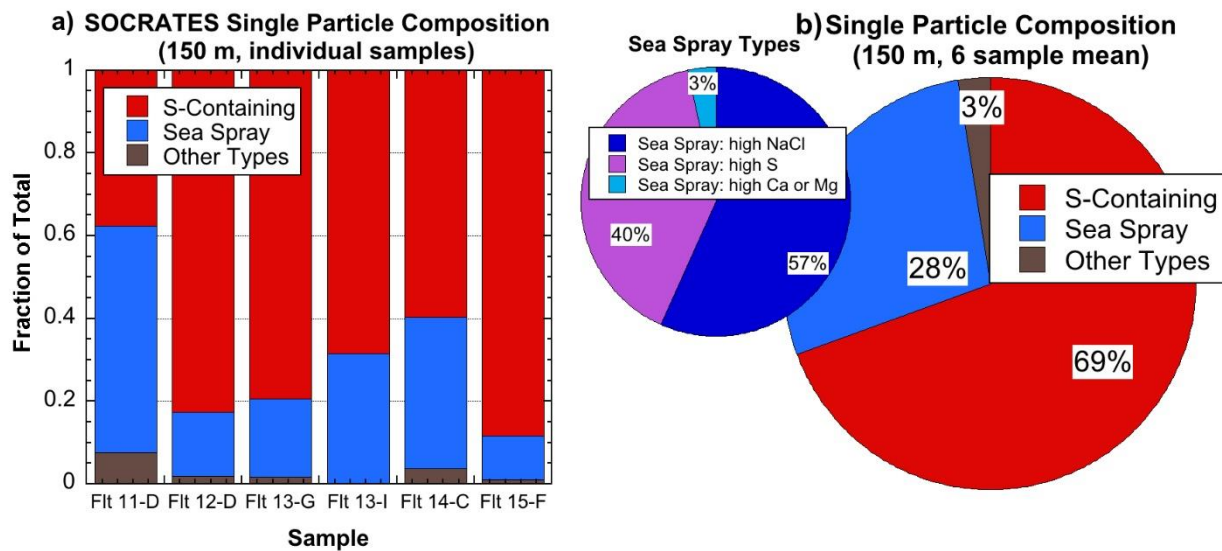
Figure 2: Normalized frequency of sampling in each 1 degree latitude bin sampled during MARCUS (green), CAPRICORN-1 (dark blue), CAPRICORN-2 (light blue), and SOCRATES (yellow). These are based on the following total number of minutes that each campaign sampled south of 43S: SOCRATES, 6,319 minutes; MARCUS; 182,470 minutes; CAPRICORN-1, 44,408 minutes; CAPRICORN-2, 60,060 minutes.



1580
1581 Figure 3: Daily mean number fraction of low volatility particles measured using the V-TDMA
1582 during CAPRICORN-1. Pre-selected particle diameters were 40 nm (blue) 100 nm (yellow) and
1583 150 nm (red). Error bars represent the standard deviation in the daily mean for each preselected
1584 particle size.

1585

1586



1587
1588 Fig. 4. a) Compositional fraction of total particles by number in the 0.1-0.5 μm dry size range for
1589 six 150 m samples on SOCRATES flights 11-15. (Sample times in UTC: 11-D: 04:41:30-04:46:30;
1590 12-D: 04:53:00-04:55:00; 13-G: 04:26:20-04:31:20; 13-I: 05:26:00-05:30:00; 14-C: 04:22:30-
1591 04:26:00; 15-F: 05:59:40-06:04:50.) Categories: *S-containing*: with S (and sometimes, O) primary
1592 elements. *Sea Spray*: Salts of Na, Cl, Mg, S, K, Ca, sometimes with organic coatings. *Other types*:
1593 includes crustal dust (silicates and carbonates), metals (Al, Fe, Cr, Ti, Mn, Co, Zn, Cu, O etc.),
1594 primary organics (C and sometimes O) and combustion particles (high S, C, O with K). b) Average
1595 composition by number for all six samples; smaller inset further subdivides *Sea Spray* into
1596 different types of salts.

1597

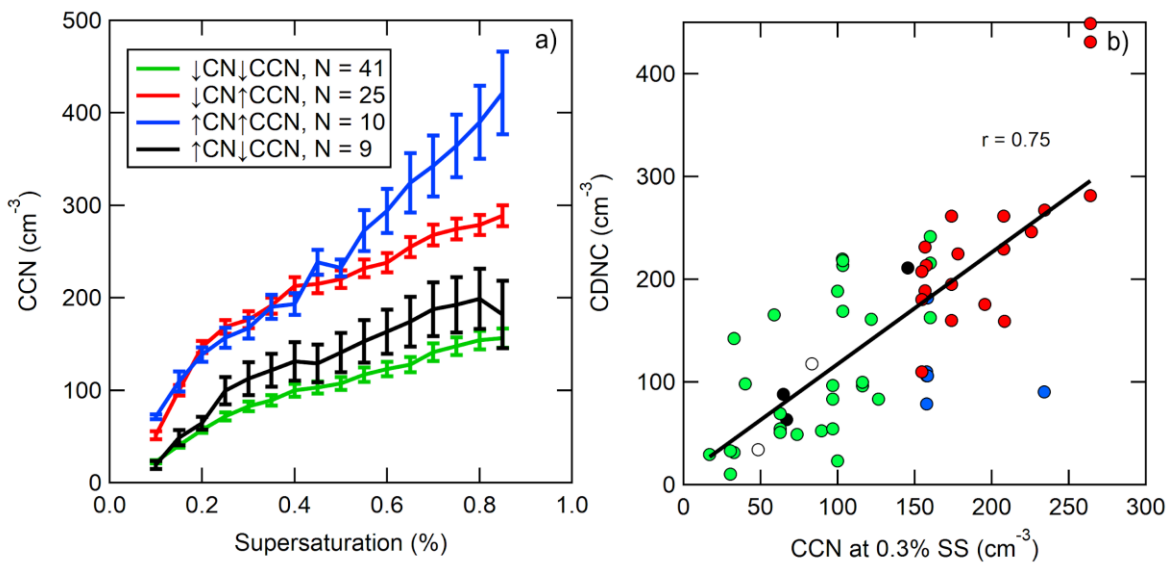
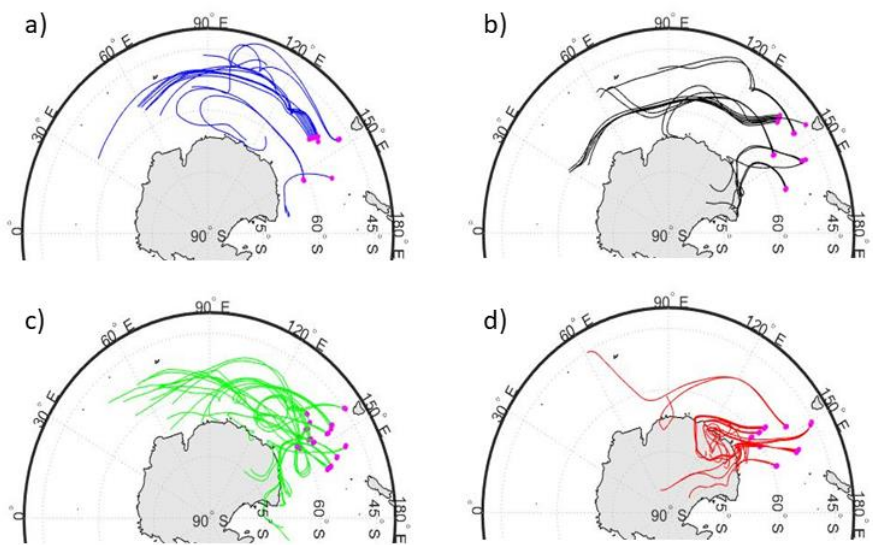
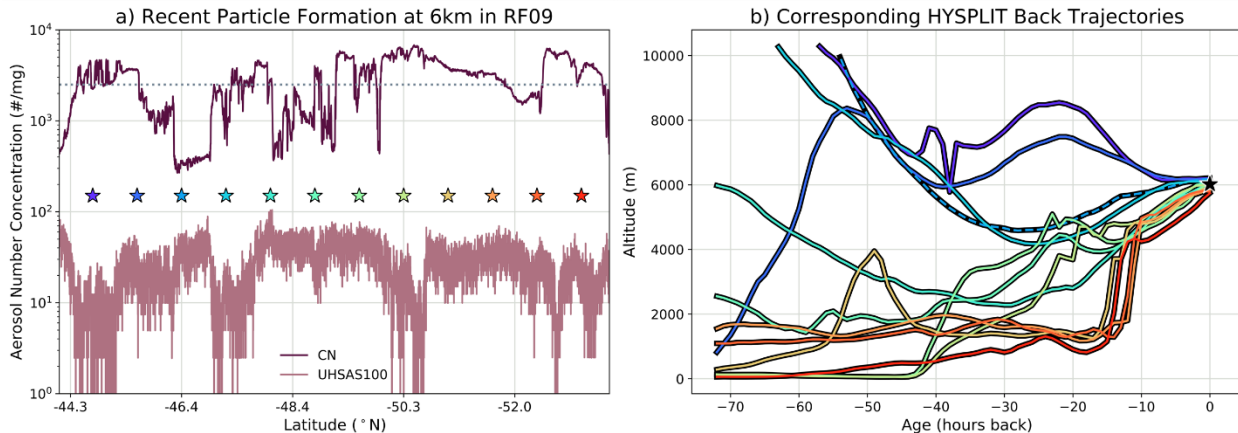


Figure 5. a) CCN spectra measured in the marine boundary layer, clustered by CN and CCN concentrations. Error bars represent the standard error. b) Measured below-cloud CCN concentrations at 0.3% supersaturation vs the observed in-cloud droplet number concentration (CDNC). The black line is a linear fit with $r = 0.75$. The same color scheme used to identify the cluster is used in both figures. The white points in (b) represent measurements that were not clustered due to missing data.



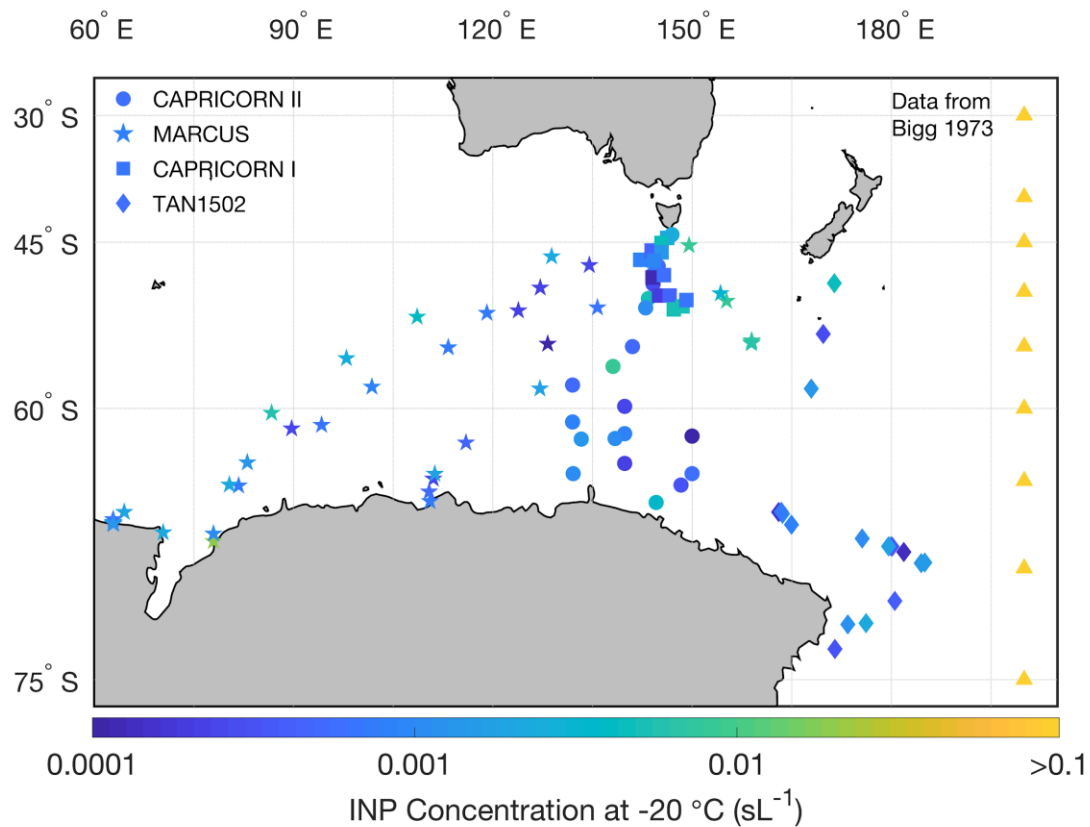
1609
 1610 Figure 6. HYSPLIT 5-day back trajectories for the four clusters shown in Figure 1, a)
 1611 High CN/High CCN, b) High CN/Low CCN, c) Low CN/Low CCN and d) Low CN/High CCN.
 1612 The magenta circles represent the HIAPER G-V location used to initialize the back
 1613 trajectory.
 1614



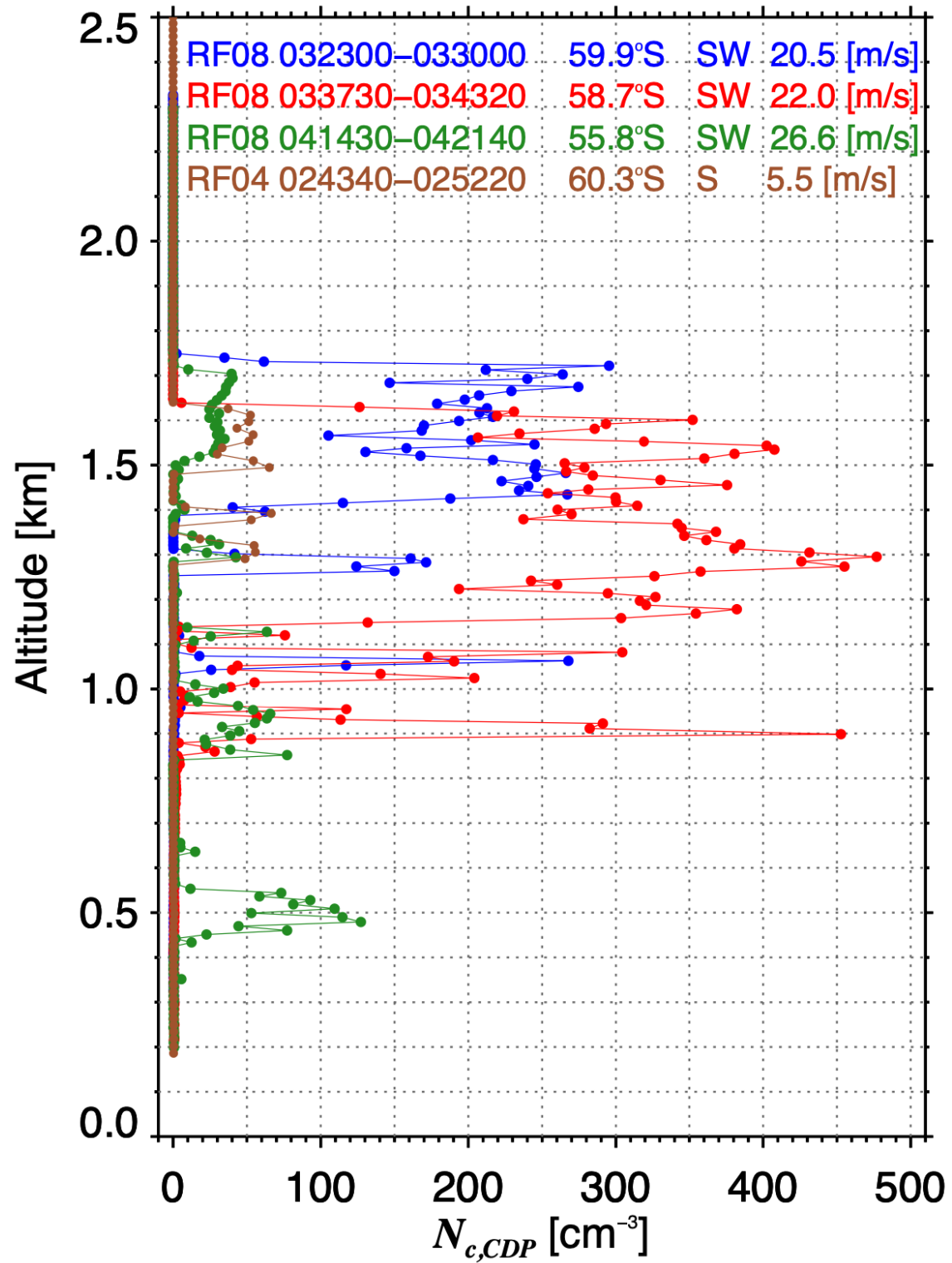
1615
1616 Figure 7 (a) Time series of total CN ($D > 11 \text{ nm}$) and accumulation mode (wing mounted UHSAS,
1617 $100 < D < 1000 \text{ nm}$) aerosol number concentrations sampled in the free tropospheric survey leg
1618 ($\sim 6 \text{ km}$) of RF09 as the GV flew south. (b) HYSPLIT 72-hour back trajectories of air masses
1619 initiated in 10 minute intervals (starred locations in (a) with color-coded matched time in (b)) along
1620 the GV flight path. Trajectories dominated by RPF events are identified by where maximum CN
1621 over the corresponding 10 minutes exceeds 2500 mg^{-1} (dotted line, (a)). In this case, only one
1622 trajectory does not satisfy the criteria for RPF events (dashed line, b). The majority of trajectory
1623 ascents exhibit synoptic uplift ($3-6 \text{ cm s}^{-1}$) within 20-30 hours of SOCRAVES sampling (star) and
1624 are in proximity to phytoplankton emissions ($Z < 1 \text{ km}$) in the prior 72 hours.

1625
1626

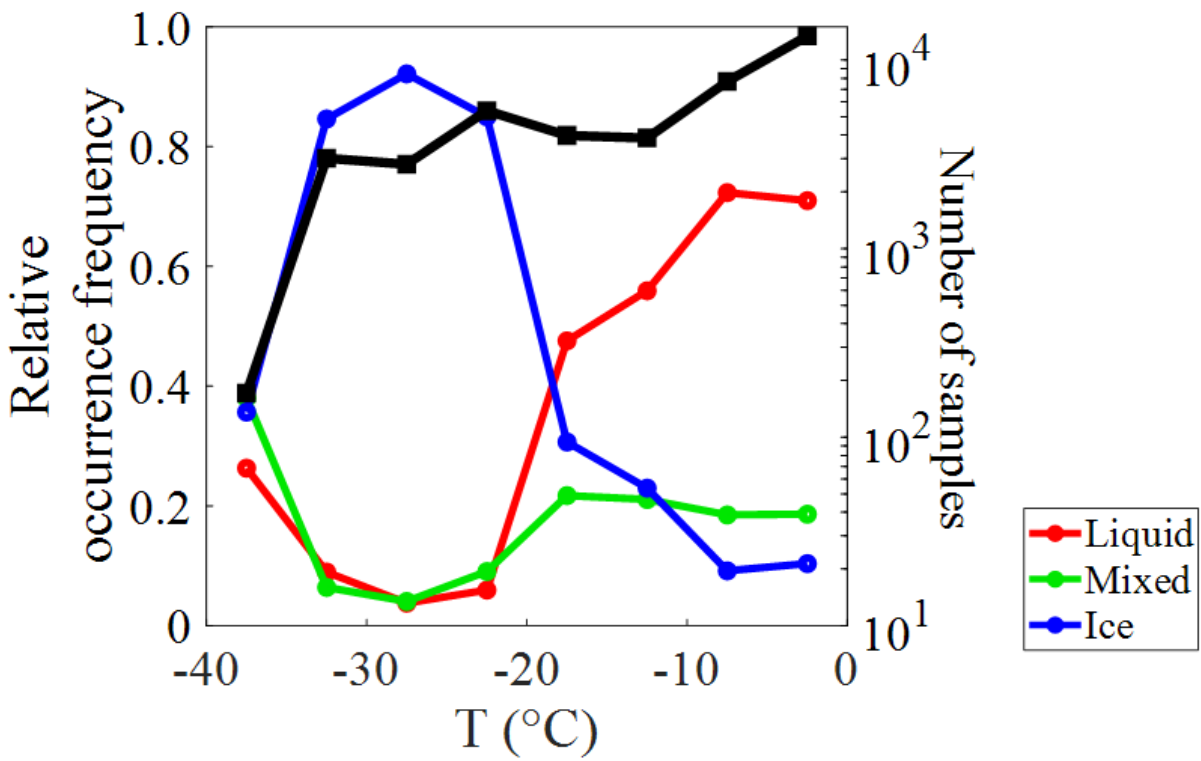
1627



1630 Figure 8. INP number concentrations per volume of air at -20°C over the SO region for a selection
 1631 of the studies (MARCUS, CAPRICORN I, CAPRICORN II, TAN1502) listed in Table S13. Each
 1632 data point represents the mid-point position of a single filter collection. Historical data from Bigg
 1633 (1973) are shown at right for context (each is the mean of numerous measures at that latitude); all
 1634 are the same color since all were $>0.1 \text{ sL}^{-1}$.
 1635



1636
 1637 Figure 9: Cloud droplet concentration measured as a function of altitude for four ramped
 1638 ascents/descents through boundary layer cloud for the days indicated in the legend. The time
 1639 period, average latitude, and average wind speed of each ascent or descent are indicated. Each
 1640 circle represents 2 sec average.



1641
 1642
 1643 Figure 10: Relative occurrence frequency of different phases derived from suite of in-situ probes
 1644 as a function of temperature (Adapted from D'Alessandro et al. 2020). Black line indicates
 1645 number of samples, giving some information about statistical significance of results.
 1646

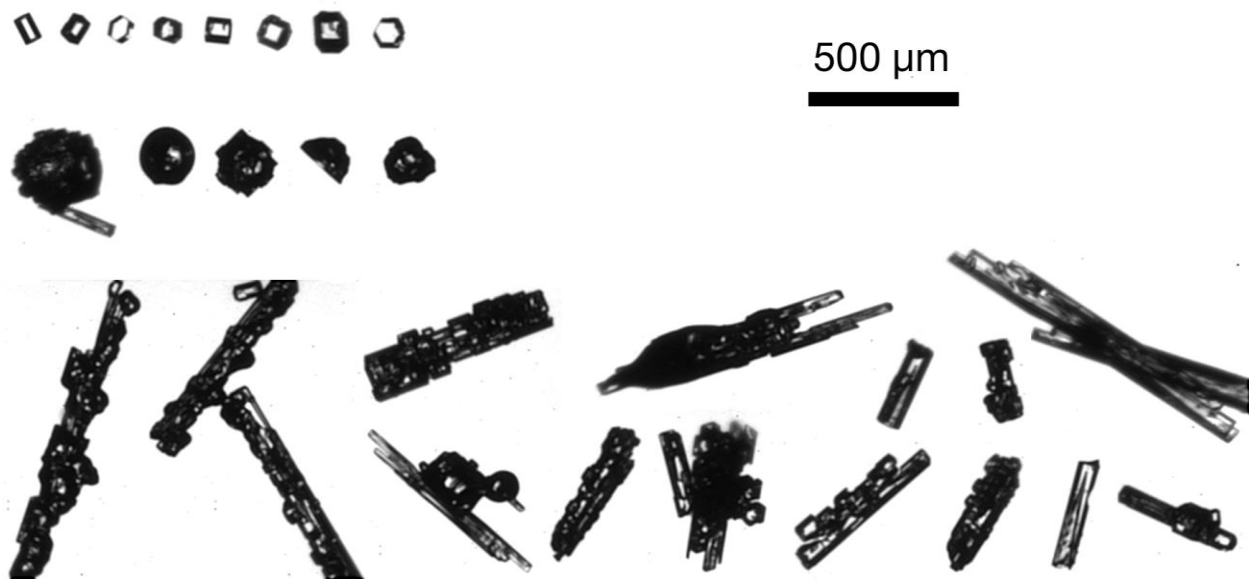
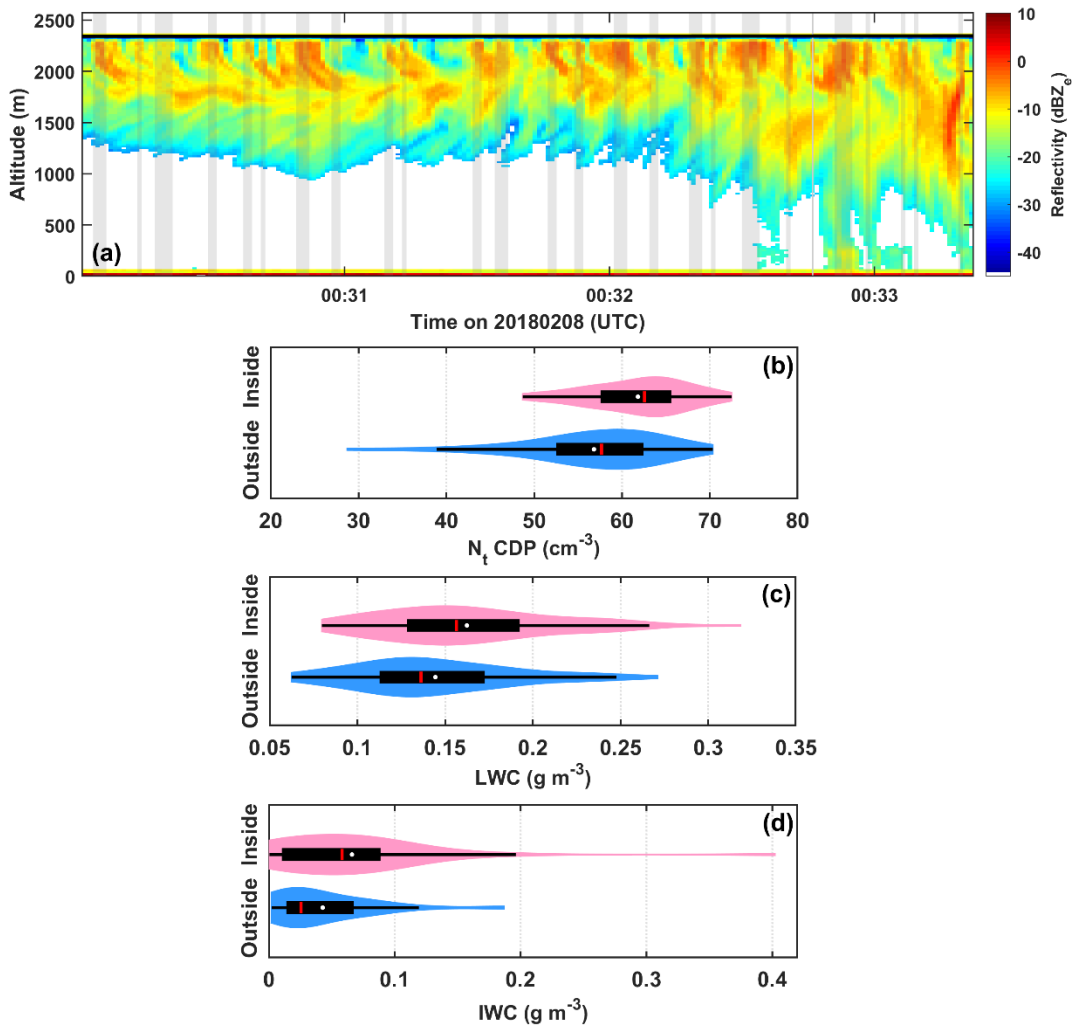


Figure 11: Collection of PHIPS images of ice particles from RF02 sampled in the temperature range 0 to -5°C.



1651

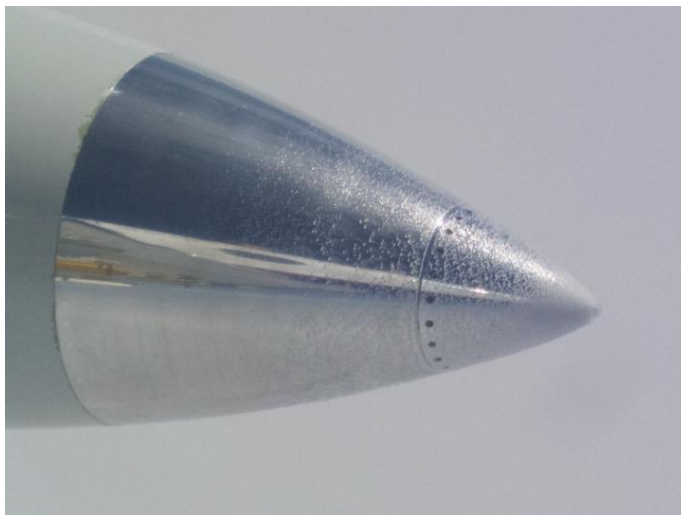
1652

1653 Figure 12: a) Altitude time-cross section of HCR Z_e over the time period between 0030 to 0034
 1654 UTC on 8 Feb. 2018. The black line shows the flight level of the G-V aircraft and the shadows
 1655 represent the location of the generating cells identified by the method of Wang et al. (2020).
 1656 Other plots show statistical analysis of data collected over this time as shown by Kernel
 1657 probability distribution functions of properties inside (pink) and outside (blue) of generating cells
 1658 for b) N_t , c) LWC and d) IWC. Black box plots show 5th, 25th, 50th (red line), 75th and 95th
 1659 percentiles of data. White point indicates mean value. Width of red and blue shaded area
 1660 represents portion of data located at particular value.

1661



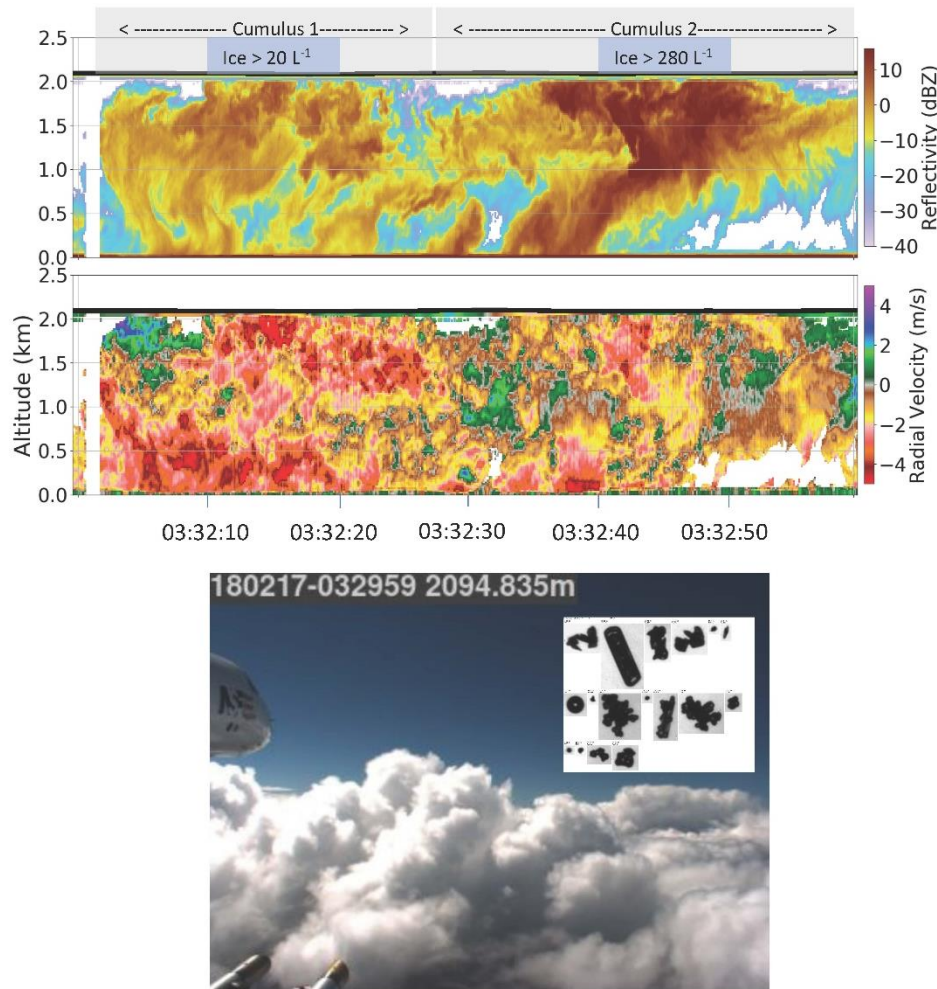
1662
1663



1664
1665

1666 Figure 13: a) The nose cone of the NSF/NCAR GV aircraft large wing pod during an encounter
1667 with small supercooled cloud droplets during SOCRATES. Ice has accreted on the tip of the pod.
1668 b) The nose cone of the GV wing pod under conditions where larger supercooled droplets were
1669 encountered. Notice the drops have impacted and run back before freezing further back on the
1670 pod.

1671

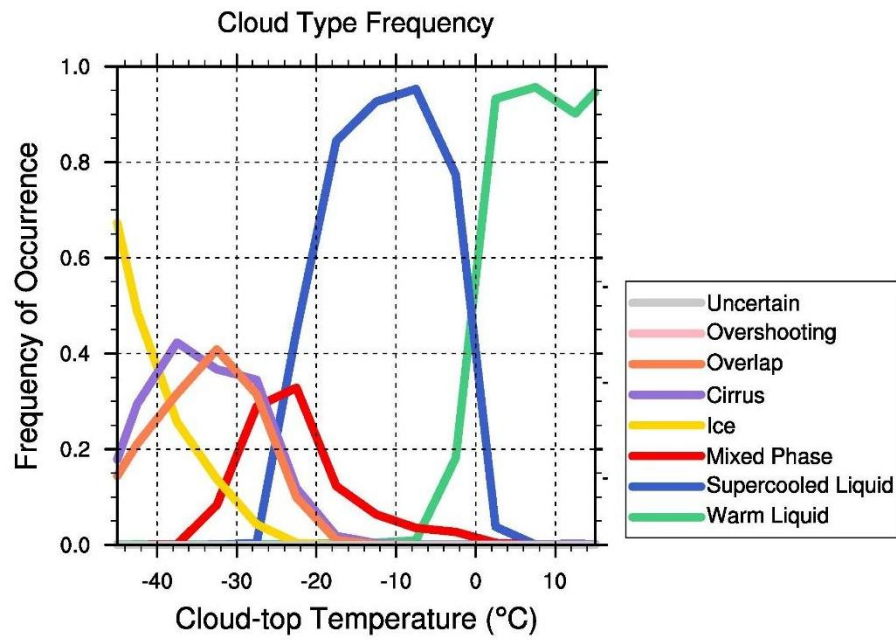


1672

1673

1674 Figure 14: Aircraft pass on 17 Feb 2018, through the tops of two closely-spaced cumuli at a
1675 temperature of -9°C , as shown by the downward-pointing airborne Doppler radar on the G-V
1676 aircraft (top two panels: radar reflectivity and vertical velocity; positive values denote upward
1677 motion of particles). Black horizontal line at top shows aircraft location as it passed through the
1678 cloud tops. Shaded gray boxes demarcate the two clouds, with shaded blue boxes identifying 10-
1679 second regions with the highest maximum ice number concentrations (corrected for possible
1680 shattering artifacts) as labeled. Snapshot from forward video (bottom panel) also shows the
1681 multiple thermal structure of these cumuli as the aircraft approached. Particle images (inset) from
1682 PHIPS probe indicated rimed ice and liquid drops were present, necessary for rime-splintering to
1683 be active, as well as the expected products of rime-splintering, pristine and rimed columns.

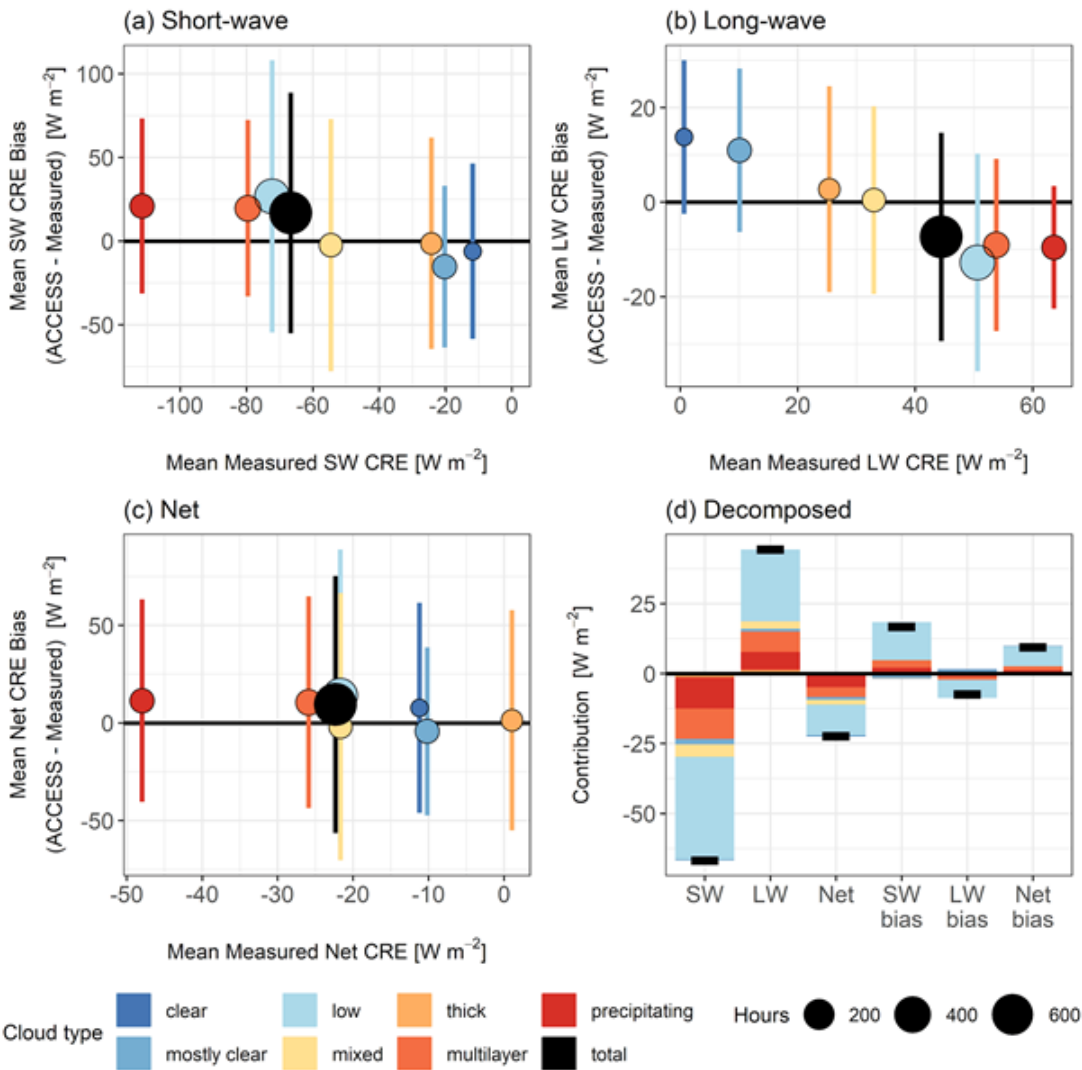
1684



1685
1686
1687
1688
1689
1690

Figure 15. (a) Flight tracks for the 15 SOCRATES missions and the outermost boundaries of the 15 sectors used for Himawari-8 analysis in (b). Frequency of occurrence of Himawari-8 cloud type as a function of cloud-top temperature for the 15 SOCRATES missions (includes times for both outbound and inbound legs).

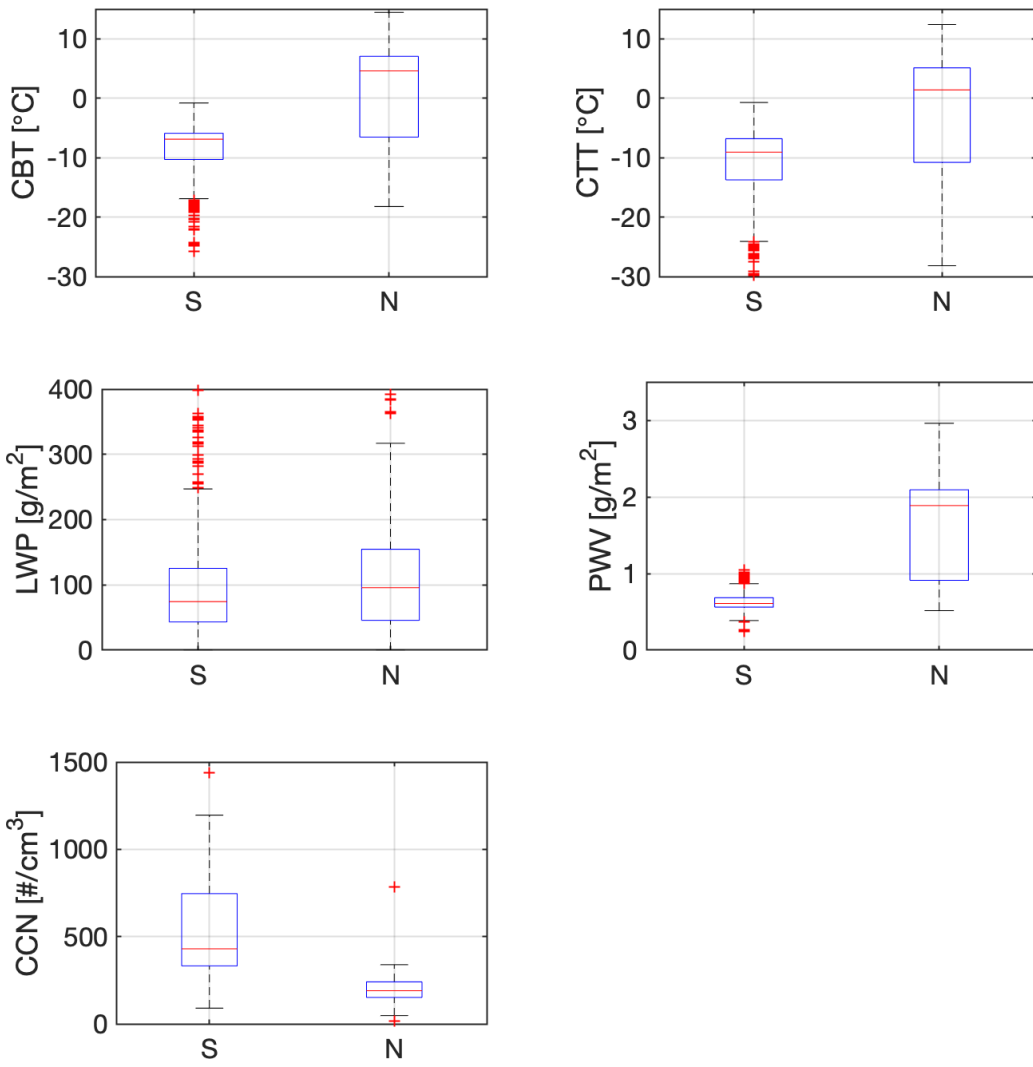
1694



1695

1696 Figure 16: The mean CRE biases ((a): short-wave; (b): long-wave and; (c): net) in ACCESS-C3
 1697 relative to the mean measured CRE for different cloud types over the Southern Ocean during
 1698 CAPRICORN I. Vertical error bars represent the standard deviation of each CRE bias for each
 1699 cloud type. The size of the points is proportional to the number of sampling hours of each cloud
 1700 type. (d) represents the decomposed CRE and CRE biases, weighted by the relative frequency of
 1701 occurrence for each cloud type. The black horizontal bars represent the total CRE and CRE
 1702 biases for the whole campaign.

1703



1704
1705 Figure 17: Statistical distribution from MARCUS cruises of how cloud and environmental
1706 properties varied depending upon whether measurements were north or south of 60°S for time
1707 periods with single-layer, non-precipitating clouds with bases less than 3 km and greater than 500
1708 km away from nearest cyclone center. Box and whisker plots show quartiles of the distribution,
1709 red line indicates mode, black bars are defined as $q_3 + 1.5 \times (q_3 - q_1)$ and $q_1 - 1.5 \times (q_3 - q_1)$,
1710 where q_1 and q_3 are the 25% and 75% percentiles, and red pluses all points outside the black bars.

1711

1712

1713

1714

1715

1716

1717

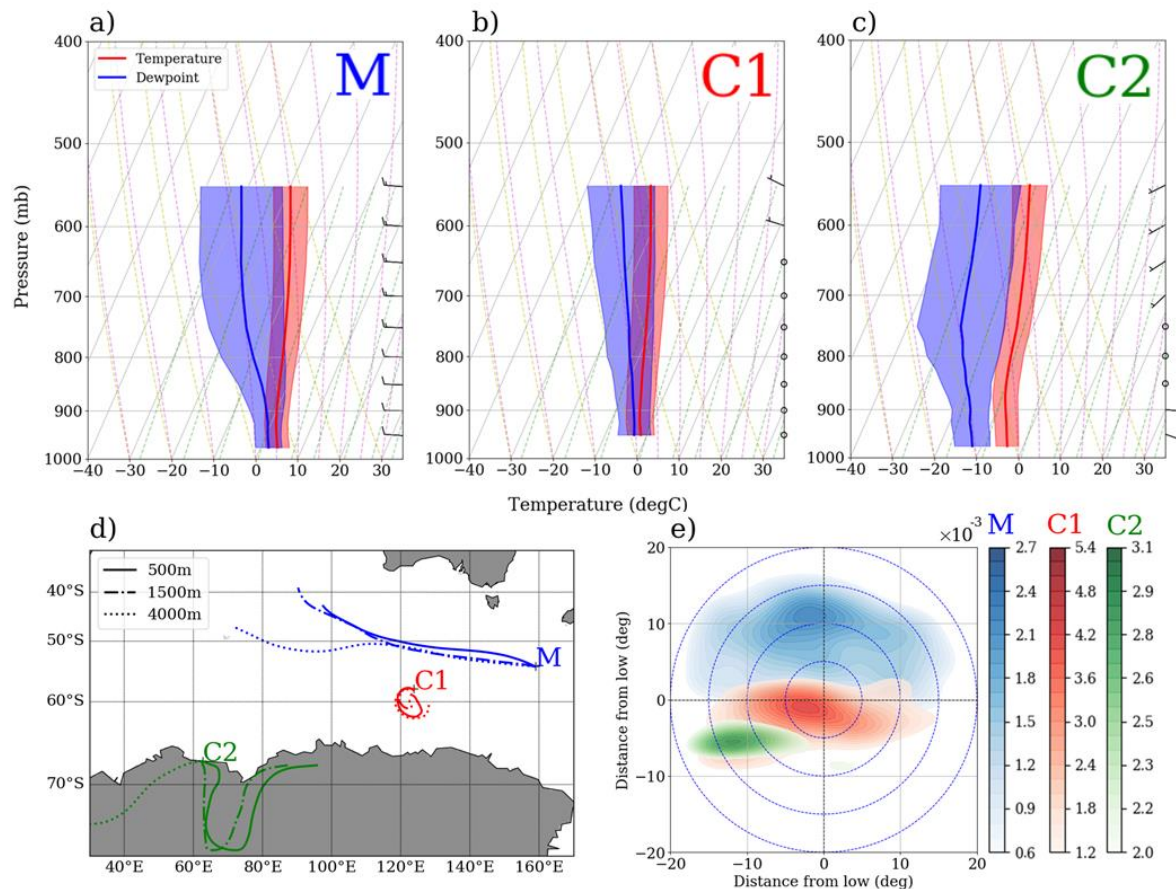
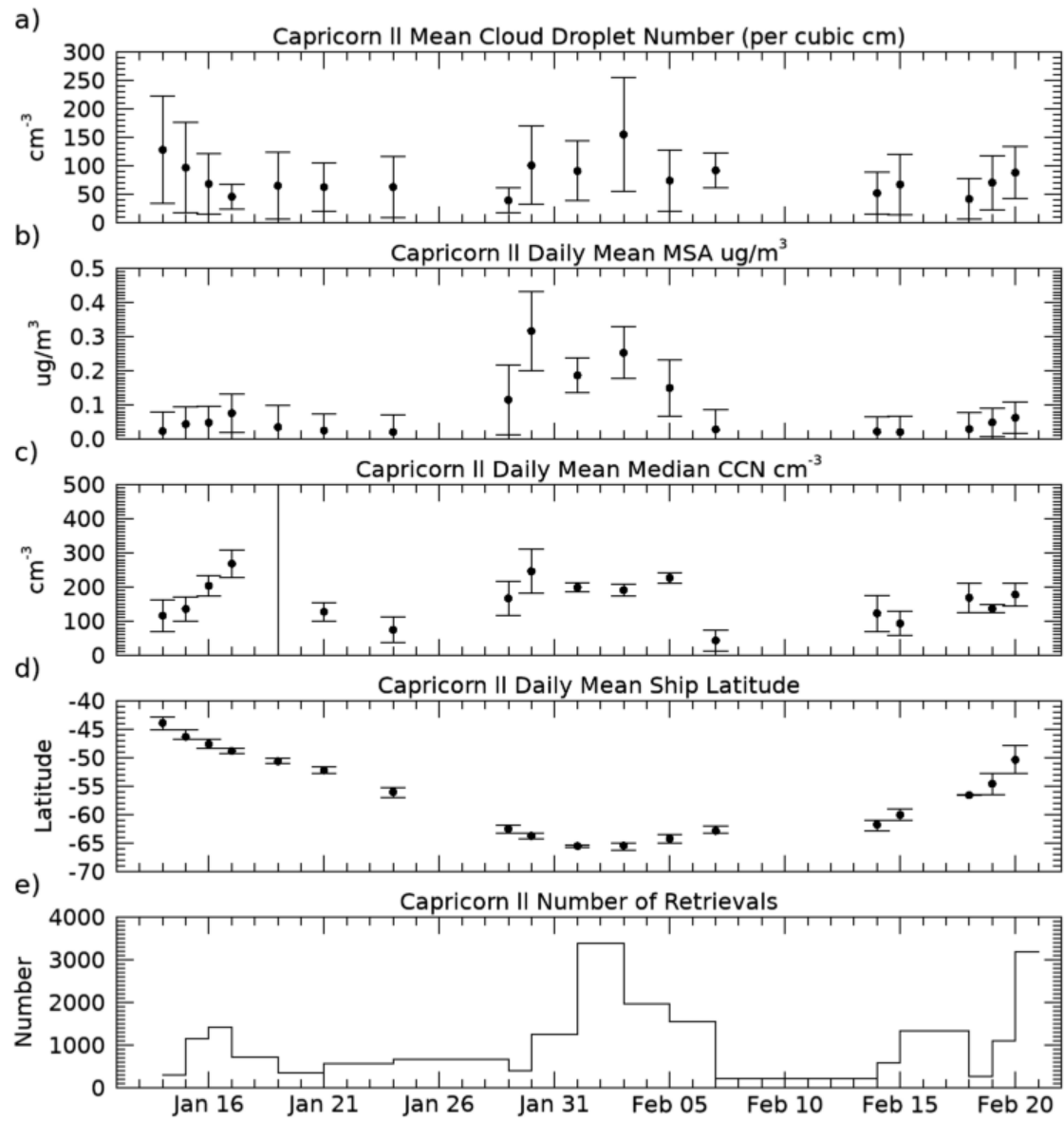


Figure 18. (a-c) Mean profiles of temperature (red line), dew point temperature (blue line) and vector wind for the clusters M, C1, and C2, respectively, displayed as a skew-T logP diagram, shaded region indicating one standard deviation. (d) 72h HYSPLIT Back trajectory for the nearest soundings to the centroid in each cluster M, C1, and C2, separately. The solid, dash-dotted, and dotted lines represent the tracks at 500, 1500, and 4000 m, respectively. (e) The frequency of occurrence composites of the sounding locations relative to the nearest cyclone centers, concentric circles indicate distances of 5°, 10°, 15° and 20° from the cyclone center.

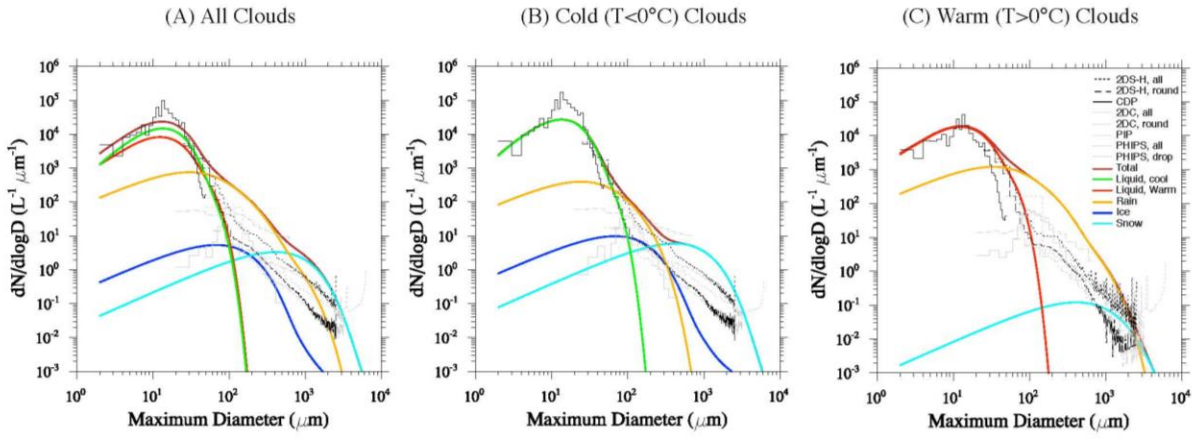
1718



1719
1720

1721 Figure 19. Daily mean derived and observed properties from the RV Investigator during
1722 Capricorn II. a) Cloud droplet number concentrations (N_c) derived for non precipitating liquid
1723 clouds using combined radar reflectivity, microwave brightness temperature, and lidar attenuated
1724 backscatter. Error bars shown standard deviation of N_c during that 24 hour period (only days
1725 with at least 200 30-second retrievals are shown), b) particulate methanesulfonic (MSA)
1726 concentrations (ug m^{-3}), c) CCN measured at 0.25% super saturation, d) latitude of the ship on
1727 that day, e) number of N_c retrievals used in the N_c means and standard deviation in panel a.
1728

1729



1730

1731 Figure 20. Size distributions from observations (thin lines) and reconstructed model hydrometeor
 1732 size distributions (thick colored lines) for low level clouds ($P > 750\text{mb}$) as indicated in the
 1733 legend. Cloud probe data shown as 2DS for all particles (black dotted), 2DS round particles
 1734 (black dash), CDP (black solid), 2DC all (gray dash), 2DC round (gray dot-dash), PIP (gray
 1735 dotted), PHIPS all (gray long dash) and PHIPS drop (gray solid). (A) All clouds, (B) Cold
 1736 clouds, (C) Warm clouds. Model is sampled along the flight track at aircraft altitude.

1737
 1738
 1739